

1 **Quantifying Particle Size and Turbulent Scale Dependence of Dust Flux in the Sahara**  
2 **Using Aircraft Measurements**

3 Philip D. Rosenberg<sup>1</sup>, Douglas J. Parker<sup>1,2</sup>, Claire L. Ryder<sup>3</sup>, John H. Marsham<sup>1</sup>, Luis Garcia-  
4 Carreras<sup>4</sup>, James R. Dorsey<sup>5</sup>, Ian M. Brooks<sup>1</sup>, Angela R. Dean<sup>6</sup>, Jonathon Crosier<sup>5</sup>, James B.  
5 McQuaid<sup>1</sup>, Richard Washington<sup>7</sup>

6 1 Institute of Climate and Atmospheric Science, School of Earth and Environment,  
7 University of Leeds, Leeds, UK.

8 2 Met Office, Exeter, UK.

9 3 Department of Meteorology, University of Reading, Reading, UK

10 4 Department of Meteorology and the Bert Bolin Centre for Climate Research, Stockholm  
11 University, Stockholm, Sweden

12 5 National Centre for Atmospheric Science, School of Earth, Atmospheric and  
13 Environmental Sciences, University of Manchester, Manchester

14 6 Facility for Airborne Atmospheric Measurements, Cranfield, UK

15 7 Department of Geography, University of Oxford, Oxford, UK

16 Corresponding author: P. D. Rosenberg, Institute of Climate and Atmospheric Science,  
17 School of Earth and Environment, University of Leeds, Leeds, LS2 9JT, UK  
18 (p.d.rosenberg@leeds.ac.uk)

19

20 **Key Points**

21 Aircraft based, size-resolved, Saharan dust fluxes are measured

22 The eddy covariance method is used with particles up to 300 micrometers

23 Links to terrain, topography and vertical turbulent kinetic energy are discussed

24

25 **Abstract**

26 The first size-resolved airborne measurements of dust fluxes and the first dust flux  
27 measurements from the central Sahara are presented and compared with a parameterization  
28 by Kok [2011a]. High frequency measurements of dust size distribution were obtained from  
29 0.16-300  $\mu\text{m}$  diameter and eddy covariance fluxes were derived. This is more than an order of  
30 magnitude larger size range than previous flux estimates. Links to surface emission are  
31 provided by analysis of particle drift velocities. Number flux is described by a -2 power law  
32 between 1 and 144  $\mu\text{m}$  diameter, significantly larger than the 12  $\mu\text{m}$  upper limit suggested by  
33 Kok [2011a]. For small particles, the deviation from a power law varies with terrain type and  
34 the large size cut-off is correlated with atmospheric vertical turbulent kinetic energy,  
35 suggesting control by vertical transport rather than emission processes. The measured mass  
36 flux mode is in the range 30-100  $\mu\text{m}$ . The turbulent scales important for dust flux are from  
37 0.1 km to 1-10 km. The upper scale increases during the morning as boundary layer depth  
38 and eddy size increase. All locations where large dust fluxes were measured had large  
39 topographical variations. These features are often linked with highly erodible surface  
40 features, such as wadis or dunes. We also hypothesize that upslope flow and flow separation  
41 over such features enhance the dust flux by transporting large particles out of the saltation  
42 layer. The tendency to locate surface flux measurements in open, flat terrain means these  
43 favored dust sources have been neglected in previous studies.

44 **Index Terms and Keywords**

45 Index terms: aerosols and Particles, turbulence; boundary layer processes; Instruments and  
46 techniques; subgrid-scale (SGS) parameterization

47 Keywords: mineral dust; eddy covariance flux; emission; topography; aircraft measurements;  
48 subgrid parameterization

49

## 50 **1. Introduction**

51 Atmospheric dust influences the globe, its atmosphere and biosphere as well as the human  
52 population in a number of ways. It affects the absorption and scattering of radiation in the  
53 atmosphere, and hence the radiation budget and heating rates. For example, it is known to  
54 affect monsoon flows [*Zhao et al.*, 2012] and the formation of tropical cyclones over the  
55 Atlantic Ocean [*Sun et al.*, 2008]. Dust can be transported long distances before being  
56 deposited and acting as a nutrient in iron limited environments [*Kaufman et al.*, 2005;  
57 *McConnell et al.*, 2008]. Dust impacts air quality and dust storms can have an economic cost,  
58 for example adversely affecting agricultural land and livestock [*Arnalds et al.*, 2001] and  
59 causing travel disruption [*Park and Lee*, 2004]. If the dust contains volcanic glass, such as  
60 those in Iceland [*Stuart*, 1927; *Arnalds et al.*, 2001], then the dust can cause an aviation  
61 hazard.

62 Airborne dust can be identified via satellite, aircraft or surface observations which may, for  
63 example, take the form of imagery, aerosol optical depths, particle size distributions, number  
64 concentrations and mass loadings. These measurements can be used to assess the success of  
65 aerosol models predicting uplift, transport and deposition; however doing so does not  
66 independently test the separate mechanisms of generation, transport and deposition of dust,  
67 which are all dependent upon particle size. Many models have similar aerosol optical depths  
68 (AODs), but widely varying emissions [*Huneus et al.*, 2011]. In order to effectively model  
69 atmospheric dust it is important to correctly predict the size dependent flux of material from  
70 the surface into the boundary layer and the free troposphere where it can be transported long  
71 distances and have significant atmospheric impact.

72 In all dust uplift models two categories of airborne particles are considered, a saltating  
73 population and a dust population [*Shao*, 2008]. Saltation particles have diameters  $\geq 100 \mu\text{m}$   
74 and can be emitted by aerodynamic forces or impacts of other saltators with the surface [*Kok*  
75 *et al.*, 2012]. Their motion after ejection is dominated by gravitational forces and they are  
76 expected to exist only in a saltation layer extending a few cm from the surface. The dust  
77 population contains much smaller and less massive particles which are more difficult to lift  
78 via aerodynamic forces due to cohesion forces in the soil, but can be ejected by saltator  
79 surface impacts and can be lifted above the saltation layer to become suspended for long  
80 durations.

81 Although wind tunnel experiments by *Alfaro et al.* [1997] and the parameterization of *Shao*  
82 [2001] indicated the presence of wind speed dependent disaggregation, *Kok* [2011b] found  
83 that field experiments [*Gillette et al.*, 1972, 1974; *Gillette*, 1974; *Sow et al.*, 2009] are not  
84 consistent with this finding and suggested the wind speed dependence was an indication that  
85 steady state emission was not reached. *Kok* [2011a] provided scale invariant model of dust  
86 emission by brittle fragmentation of aggregates of dust particles in the soil which was found  
87 to be in excellent agreement with measured emitted particle size distributions.

88 In this paper we present measurements of the size resolved dust fluxes retrieved from aircraft  
89 measurements throughout the depth of the boundary layer in the heart of the Saharan Desert.  
90 These were made as part of the Fennec project. To our knowledge these are the first  
91 measurements of size resolved dust fluxes to be made from an aircraft. The Fennec project  
92 investigated the relationship between dynamics, dust and radiation in the Earth's deepest  
93 boundary layer under the unique conditions of the Saharan heat low [*Cuesta et al.*, 2009] and  
94 included deployment of eight automatic weather stations [*Hobby et al.*, 2013], 2 supersites  
95 [*Marsham et al.*, 2013; *Todd et al.*, 2013] and sixteen flights by the UK's BAe-146-301  
96 Atmospheric Research Aircraft operated by the Facility for Airborne Atmospheric  
97 Measurements (henceforth the FAAM BAe-146).

98 As the measurements used here are taken from an airborne platform the derived values do not  
99 directly represent surface emissions. However, a number of objectives are achievable from  
100 the air and the aims of this paper are therefore as follows.

- 101 1) To provide a detailed methodology of the size resolved particle flux measurement  
102 technique used here with a description of the challenges specific to the platform and  
103 the conditions.
- 104 2) Evaluate the dependence of the flux upon particle size, covering a broader range of  
105 sizes than covered in existing literature.
- 106 3) Evaluate if or how fluxes are affected by different meteorological conditions and  
107 regional or local surfaces types.
- 108 4) Understand these results in terms of the emission processes which generate the  
109 observed dust fluxes.

## 110 2. Methods

111 The dust flux estimates presented here are derived using the eddy covariance method. Details  
112 of the instrumentation and methodology are presented below. The use of the aircraft platform  
113 permitted measurements in the heart of the Sahara where ground based observations are  
114 sparse or non-existent. It also enabled measurements over a variety of different locations and  
115 surface types and allowed us to target meteorological events of interest. However the  
116 measurements are made significantly above ground level. The minimum altitude at which the  
117 aircraft was capable of safely flying was a function of visibility such that if the pilots were  
118 able to clearly see the surface the aircraft was permitted to fly at approximately 100 m above  
119 ground level, tracking topography to maintain this altitude. However if at any point the  
120 ground was obscured by dust then the aircraft was forced to climb to the local Minimum Safe  
121 Altitude defined by maps of the local topography. This was generally of the order 1 km. The  
122 finite height above ground of the measurement platform means that the fluxes derived are not  
123 directly representative of surface emission, however the flux measured by the aircraft, which  
124 was generally in the lowest 20% of the boundary layer, is clearly strongly related to the  
125 emission flux and this relationship is discussed later in the manuscript. In some cases the  
126 altitude, combined with a moving platform can be an advantage. For example a single surface  
127 flux tower in a hilly region may be biased by its immediate surroundings, whereas an aircraft  
128 flying over a hilly region is able to average over many hills and valleys in the varying  
129 topography.

## 130 **2.1. Instrumentation**

131 The FAAM BAE-146 was equipped with a broad range of instrumentation for making in-situ  
132 measurements of the dust population. Here we use optical particle counters (OPCs), which  
133 determine the size distribution of airborne particles via the light scattered from individual  
134 particles and optical array probes (OAPs) which image the shadow of larger particles to  
135 derive size distributions. *Ryder et al.* [2013b] provides a full list of the instrument suite.

136 Three particle sizing instruments have been utilized as part of this work on the basis of their  
137 reliability and sampling frequency. These are the Passive Cavity Aerosol Spectrometer Probe  
138 (PCASP), the Cloud Droplet Probe (CDP) and the Cloud Imaging Probe (CIP) which are an  
139 OPC, an OPC and an OAP respectively. The PCASP and CDP were found to work well  
140 throughout the Fennec detachment, although there may have been a calibration problem with  
141 the small sizes measured by the PCASP so the first 7 channels (up to  $\sim 0.16 \mu\text{m}$  diameter, all  
142 affected by one amplification stage) of this instrument have been omitted as a precaution. In

143 combination these three instruments provide size distributions covering particle diameters  
144 ranging from  $\sim 0.16 - 960 \mu\text{m}$ . An important characteristic of these particle sizing instruments  
145 is their sampling frequency. The smallest eddy scale which may be captured by the flux  
146 derivation is twice the ratio of the aircraft airspeed (approximately  $120 \text{ m s}^{-1}$ ) to the  
147 instrument sampling frequency. The PCASP has a sampling frequency of 10 Hz giving a  
148 minimum resolvable length scale of approximately 24 m. The CDP gives a 1 ms resolution  
149 timestamp for the first 256 particles detected each second (which is sufficient to timestamp  
150 every dust particle measured in this work) and the CIP timestamps every one of its images  
151 with  $0.125 \mu\text{s}$  resolution. The data from these two instruments were bin-averaged to match  
152 the 10 Hz PCASP data.

153 The CIP was manufacturer calibrated using a spinning disk which passes different sized dots  
154 through the laser. Both the PCASP and CDP were calibrated before and after Fennec. In  
155 addition the CDP was calibrated on each flying day. Some drift was observed in the PCASP  
156 calibrations and the uncertainties used here take this into account. No drift was observed in  
157 the CDP calibrations. Because the CDP and PCASP make measurements based upon the  
158 optical properties of particles there is a dependence upon the refractive index and shape of the  
159 particles. Here these factors are accounted for by assuming spherical particles and Mie  
160 theory. The calibrations and the optical property corrections utilize the methods of *Rosenberg*  
161 *et al.* [2012]. The particle refractive index used was  $1.53+0.001i$  which gave the best  
162 radiative closure between the OPCs and the aircraft nephelometer [*Ryder et al.*, 2013b].  
163 When converting from particle diameter to particle mass the equations for the volume of a  
164 sphere are used, then multiplied by the product of an assumed density and shape factor  $\rho S$ .  
165 Here we take  $\rho S = 2.12 \text{ g cm}^{-3}$  as reported by *Sow et al.* [*Sow et al.*, 2009], however we do so  
166 noting that it is unclear whether the OPC data upon which this value is derived was corrected  
167 for particle refractive index and also that other authors have used different measured or  
168 assumed values (e.g.  $2.4 \text{ g cm}^{-3}$  [*Gillette et al.*, 1974],  $2.65 \text{ g cm}^{-3}$  [*Tegen and Fung*, 1994]).

169 For wind measurements the FAAM BAe-146 utilizes a radome mounted 5-port pressure  
170 transducer based turbulence probe [*Petersen and Renfrew*, 2009] for angle of attack  
171 measurements and a pitot probe for airspeed measurements which allows derivation of  
172 aircraft relative 3-D wind vectors. These are combined with data from a GPS inertial  
173 navigation unit to provide surface relative winds. This system provides measurements at 32  
174 Hz, although here the data has been resampled to provide 10 Hz data matched to the PCASP.

175 After the campaign it was found that there was a small linear dependence between measured  
176 vertical wind speed and aircraft attitude. This dependence was likely caused by a small error  
177 in the calibration of a transducer and was removed by subtracting a linear fit.

## 178 **2.2. Eddy Covariance Flux Measurements**

179 The eddy covariance method has been previously used to derive heat, moisture and  
180 momentum fluxes from aircraft measurements [e.g. *Brooks and Rogers, 2000; Petersen and*  
181 *Renfrew, 2009*] and a number of different fluxes including total aerosol number from the  
182 ground [*Dorsey et al., 2002*]. Here the same method is used to derive size resolved dust  
183 fluxes using aircraft measurements. To do so the vertical wind and dust number or mass  
184 concentration are separated into a mean value and a deviation from the mean by way of  
185 Reynolds decomposition. When applied to dust measurements the appropriate  
186 decompositions are

$$187 \quad p(t) = \bar{p} + p'(t), \quad (1)$$

188 where  $p$  is a placeholder for vertical wind component,  $w$ , dust number concentration,  $n$ , or  
189 dust mass concentration,  $m$ . Barred symbols represent the mean over a fixed time period and  
190 dashed symbols represent the perturbation from the mean over the same period. The flux of  $n$   
191 is then related to the covariance of  $n$  and  $w$  such that

$$192 \quad F_n = \overline{w'(t)n'(t)}, \quad (2)$$

193 with an equivalent equation for dust mass concentration,  $m$ . In this work we perform a linear  
194 detrend of the data before the Reynolds decomposition and we time-shift the concentration  
195 data by a small amount (less than 1 s) in order to account for position offsets of the  
196 instruments along the airframe and maximize the cross correlation with the winds.  
197 Detrending reduces contamination of the turbulent flux estimate by mesoscale variations.  
198 Because material that has been transported long distances will be well mixed within the  
199 boundary layer it will provide small values of  $n'(t)$ , which will not be correlated with  $w'(t)$  so  
200 will provide negligible flux contributions. However, due to the height of the measurements,  
201 some dust transport will occur before the measurements are made. This will certainly affect  
202 the magnitude of the dust fluxes measured, and have the potential to affect the largest sizes  
203 which may succumb to gravitational settling.

204 Some limitations to the eddy covariance method are particularly relevant to the aircraft  
205 platform and the Saharan boundary layer. High frequency measurements are required so that  
206 small eddy scales are sampled. As the aircraft is travelling at approximately  $120 \text{ m s}^{-1}$  and the  
207 instrument sampling period is 0.1 s we only sample eddies with sizes  $\gtrsim 24 \text{ m}$ . It is also of  
208 note that turbulent scales are likely to be larger at the aircraft altitude than at ground level.  
209 The flight leg over which one flux derivation is made must be long enough to span multiple  
210 eddies at the largest eddy scales and to provide sufficiently good counting statistics for the  
211 dust measurements. As the Saharan boundary layer can be 5 km deep and the mass  
212 concentration may be dominated by a relatively small number of large particles, this can  
213 require legs of 50-100 km. Finally, the measurement area should be homogeneous or at least  
214 mesoscale variations should be linear with distance. It is clear that there is a trade-off  
215 between these requirements as longer legs are more likely to encounter mesoscale variations.  
216 In order to achieve the best flux estimates the following principles have been followed. The  
217 flight data has been carefully selected to avoid mesoscale variation where possible. Care has  
218 been taken to derive rigorous uncertainties for the dust flux measurements. Where these are  
219 high, size resolved estimates have not been utilized.

220 In order to ensure that both the largest and smallest eddy scales have been measured we plot  
221 an ogive curve for each flux leg [*Brooks and Rogers, 2000*]. The ogive is the cumulative  
222 integral of the cospectral density, so it is steepest for eddy scales which make a large  
223 contribution to the flux. The cospectrum is not used directly because it is noisy, making it  
224 difficult to identify the contributing length scales. The integration performed to create an  
225 ogive quickly provides a signal which is larger than the noise and the signal to noise ratio  
226 continues to improve along the curve. This means an ogive can be usefully plotted on a linear  
227 vertical scale and the ogive has therefore become the de-facto standard for analyzing scale  
228 dependence of fluxes. If the turbulence is well behaved and all relevant length scales are  
229 measured, the ogive should be flat at both ends (the largest and smallest scales) where  
230 contributions to the flux are negligible. Here all ogives are normalized to unity at the largest  
231 length scales.

232 One potential problem with measurements of particle fluxes is the non-negligible mass of  
233 large particles. There is therefore a downward flux of particles caused by gravitational  
234 settling and a deviation of particle velocities from the atmospheric turbulent motion. The  
235 fluxes here exclude gravitational settling as this is a deposition process assessed separately in



236 models and the flux from this process is additive. However, we do require a framework to  
237 assess the importance of particles not following turbulent motion, which we derive as  
238 follows. Considering a stationary particle which is exposed to an eddy of diameter  $s$   
239 providing an updraft speed  $w$ , the air traverses the eddy in a time  $t \approx s/w$ , by which time the  
240 particle lags the air by a distance

$$241 \quad \Delta s = w\tau(1 - \exp[-t / \tau(d)]), \quad (3)$$

242 where  $\tau(d)$  is the aerosol relaxation time as a function of its diameter as per the standard  
243 definition for this parameter. The average speed of the particle over this time is then given by  
244  $(s - \Delta s)/t$ . The inertial correction factor is simply the ratio of the mean particle velocity to the  
245 air velocity which, from the above, is found to be

$$246 \quad c_{in} = 1 - \frac{1 - \exp(-R)}{R}, \quad (4)$$

247 where we define  $R$  as the particle-eddy interaction parameter given by  $s/(w\tau(d))$ . Physically  
248 the eddy influence can be considered as the dimensionless aerodynamic impact that an eddy  
249 has upon the trajectory of an aerosol particle. As  $R$  increases from zero the turbulent motion  
250 has an increasing effect upon the particle trajectory. As one would expect,  $R$  increases with  
251 increasing eddy size and decreasing particle relaxation time (and hence mass) and vertical  
252 velocity.  $c_{in}$  approaches unity asymptotically as  $R$  increases, and is zero when the eddy  
253 influence is zero. For values of  $R$  greater than 20,  $c_{in}$  is greater than 0.95. As will be discussed  
254 later in this paper  $c_{in}$  is always close to unity for the measurements presented here and is  
255 therefore neglected.

### 256 **2.3. Satellite and Model Products**

257 In order to effectively interpret the results, data from the Meteosat Second Generation  
258 mounted Spinning Enhanced Visible and Infrared Imager (SEVIRI) red-green-blue thermal  
259 infrared dust product and Operational forecasts from the Met Office Africa Limited Area  
260 Model (Africa LAM) were used. These allow the data to be placed in wider scale context.  
261 The SEVIRI dust product images presented here show dust as a bright pink color [Brindley *et*  
262 *al.*, 2012]. However the surface is similarly colored to the dust in some locations and the  
263 dust-surface contrast depends in part upon temperature contrast and therefore dust height.  
264 The dust becomes much more obvious in animations where it can be seen to move against the

265 stationary background. The Africa LAM is a regional simulation using the Met Office  
266 Unified Model (UM) [Lock *et al.*, 2000; Davies *et al.*, 2005] and has a 12 km horizontal grid-  
267 spacing at the equator and 70 vertical levels. Here it is used to provide estimates of near  
268 surface horizontal wind.

#### 269 **2.4. Uncertainty Calculations**

270 Because of the discrete nature of the particle measurements, counting uncertainty represents a  
271 significant contribution to the total uncertainty of the particle concentration, and hence flux.  
272 When considering mass flux, this is often the dominant uncertainty source. The contribution  
273 by all random uncertainties, including counting uncertainty and noise in the turbulent velocity  
274 data, can be assessed by the method described by *Billesbach* [2011]. To do so the  
275 concentration measurements are shuffled, which provides a dataset that is uncorrelated with  
276 the vertical winds but follows the same probability density function as the unshuffled data.  
277 The standard deviation of the cross correlation series of the shuffled data with the vertical  
278 winds is equal to the noise level and hence the random uncertainty. The other major  
279 contributor to the dust mass flux is the derivation of the mass per particle. As discussed above  
280 this is a function of the uncertainties in particle optical properties, shape and density and  
281 generates a systematic uncertainty which is likely to be of the order 25 %.

#### 282 **3. Synoptic and Geographic Background of the Observed Dust Uplift Cases**

283 Sixteen flights were carried out during Fennec in 2012, eleven of which included  
284 measurements in the heavily dust laden boundary layer. Dust flux measurements from five  
285 flights are presented here. These flights were chosen because the flight patterns used and the  
286 conditions observed permitted measurement of statistically significant dust fluxes. The tracks  
287 of these five flights, along with their flight reference numbers are shown in Figure 1; flight  
288 times, locations and observed conditions are summarized in Table 1. Also labeled on Figure 1  
289 are geographical features which influence dust uplift in the region.

290 Geography clearly has a significant impact upon dust uplift, for example by orographic  
291 channeling of winds, which has previously been implicated in erosion on various scales  
292 [Washington *et al.*, 2006; Netoff and Chan, 2009], and by determining availability of erodible  
293 material [Schepanski *et al.*, 2013]. The descriptions here are based on in-flight observations,  
294 satellite imagery, the Africa AMS Topographic Map Series and information from  
295 Mauritanian colleagues. Regueibat Rise is an elevated region of bright terrain in northern

296 Mauritania. It is relatively flat with some shallow broad drainage channels running across the  
297 surface. A line of dunes penetrate the region from the northeast. Very sparse low scrub was  
298 observed over the region, particularly in preserved vehicle tracks, implying that the surface  
299 has a low erodability. Regueibat Rise is bordered to the south by a dark series of linear ridges  
300 and waddis known as El Hank. The dried up drainage channels here provide a source of loose  
301 material and potential for channeling of winds. Some bright mineral deposits in dried lake  
302 beds were also observed here. Immediately to the south of El Hank is the Erg Chech sand sea  
303 which then blends into the El Djouf Desert. The Erg Chech dunes are oriented approximately  
304 NE with spacings of ~1-10 km. Between the dunes, non-sandy dark surface is visible, as are  
305 some bright dry lake beds. In Mali at the north-eastern edge of El Djouf is a basin bordered to  
306 the north and east by ridges known as Hamada Safia and Hamada El Haricha. Close to Erg  
307 Chech, the El Djouf Basin also consists of sand sea, but with closer spaced dunes. Moving  
308 southward the dunes become sparser and disappear. All these regions were overflown by the  
309 FAAM BAe 146 during Fennec, providing data over sand seas, dry river and lake beds, stable  
310 soil and steep and shallow terrain.

311 The meteorology of all five flights was influenced by nocturnal low level jets (LLJs). LLJs  
312 are formed in this region when deep dry convection halts in the evening, reducing downward  
313 momentum transport and therefore reducing the impact of friction upon the lower boundary  
314 layer. The resulting force imbalance causes an oscillation about the new equilibrium point,  
315 creating a supergeostrophic jet at altitudes of approximately 500 -1000 m [*Blackadar, 1957*;  
316 *Van de Wiel et al., 2010*]. After sunrise dry convection resumes, mixing the momentum of the  
317 jet down towards the surface, which increases both mean wind speed and gustiness [*May,*  
318 *1995*; *Knippertz, 2008*]. This plays an important role in dust uplift due to the nonlinear  
319 relationship with the friction velocity. LLJs are a common feature in the Sahara in Summer  
320 [*Fiedler et al., 2013*; *Marsham et al., 2013*; *Todd et al., 2013*]. *Schepanski et al* [2009] found  
321 that 65% of satellite observed dust emission events occur in the 0600-0900 UT period  
322 consistent with the time of LLJ breakdown, however this can be regarded as an upper  
323 estimate as other dust uplift mechanisms are associated with clouds, prohibiting satellite  
324 identification [*Heinold et al., 2013*; *Kocha et al., 2013*]. Here, LLJs have simply been  
325 identified from the Africa LAM as morning peaks in wind speed between the surface and  
326 1500 m altitude around the Saharan heat low which mix away during the day. The fact that all  
327 flights presented here are related to LLJ dust uplift does not imply that these are the dominant  
328 dust uplift mechanism in the region. The synoptic scales of LLJs make them relatively easy to

329 forecast, easy to target with flights and easy to collect data under homogeneous conditions. In  
330 contrast dust uplift events caused by cold pool outflow from mesoscale convective systems,  
331 known as haboobs, cannot be easily forecast by models with parameterized convection  
332 [Marsham *et al.*, 2011]. This makes them difficult to target. They also exhibit significant  
333 heterogeneity [Solomos *et al.*, 2012] making flux derivations difficult.

334 Three of the five flights (B600, B601 and B602) occurred on 17<sup>th</sup> and 18<sup>th</sup> June 2011 and  
335 each followed a very similar flight track. The meteorology on these two days was also  
336 similar, with the Africa LAM forecasting a broad scale Harmattan Wind linked to a LLJ  
337 flowing from Algeria into northern Mauritania and Mali as seen in Figure 2. On the morning  
338 of 17<sup>th</sup> June the wind speed was above 7 m s<sup>-1</sup> up to 3 km, with a 16.5 m s<sup>-1</sup> maximum at 1  
339 km. On the 18<sup>th</sup> June a similar wind maximum at 1 km and a second wind maximum at 3 km  
340 were forecast. In contrast the forecast for midday on the 17<sup>th</sup> shows a much more well-mixed  
341 profile. The aerosol optical depth at 550 nm (AOD) measured during the descent was much  
342 lower for flight B602 (Table 1). The three flights all consisted of a high level transit followed  
343 by descent to the minimum permitted altitude at the farthest southeast point, then a return to  
344 the northwest at low level. During flights B600 and B601 visibility was poor close to the  
345 surface, and the low level legs were at altitudes of between 700-800 m. However the aircraft  
346 was able to descend briefly to 500 m during B601. During B602 visibility was better and the  
347 low level leg was performed at 100 m above the ground.

348 Flight B610 probed the decay of another forecast LLJ on 25<sup>th</sup> June 2012 over northeast  
349 Mauritania during the period just after dawn as seen in Figure 3a). Two reciprocal low level  
350 legs were performed at the expense of covering a smaller geographic region than during  
351 flights B600-B602. Visibility permitted these legs to be made at 100 m above ground level.  
352 Again an upper level (4 km) wind maximum was forecast and observed by the aircraft in  
353 addition to the 18 m s<sup>-1</sup> LLJ maximum as seen in Figure 3b. This time the LLJ was less  
354 geographically expansive and further north, encompassing the El Hank and Regueibat Rise  
355 regions.

356 The final case considered here is flight B613 which consisted of a series of stacked legs in the  
357 boundary layer in the afternoon of 26<sup>th</sup> June. This flight was at the far western extent of an  
358 east-west LLJ identified in the 0900 Africa LAM forecast (not shown). At the flight location  
359 the 0900 forecast indicated two low level wind maxima (not shown), both of which were  
360 weaker than those forecast for the previous cases. The first was of 10 m s<sup>-1</sup> at 1200 m altitude

361 and the second of  $7.5 \text{ m s}^{-1}$  below 500 m altitude. The winds at the flight time were forecast  
362 to be only  $3 \text{ m s}^{-1}$  on the lowest model level and well mixed throughout the boundary layer as  
363 shown on Figure 3c and 3d. The measurements indicated a slightly larger mean wind speed  
364 than forecast and also a positive gradient in wind speed with altitude which was not forecast.  
365 The gustiness of the wind was particularly notable in this case with  $5 - 10 \text{ m s}^{-1}$  peak-to-peak  
366 variations of the wind speed within the boundary layer. Because dust uplift is highly  
367 nonlinear and is generally modeled as being proportional to wind speed cubed once the wind  
368 speed has exceeded a threshold, this gustiness is important for potential dust uplift.

#### 369 **4. Results and Discussion**

370 The results presented here include both size resolved and total fluxes. We first present the  
371 size resolved results, then discuss how this size resolved data can be used to link the flux to  
372 surface emission. We then present the total fluxes derived by integration of the size resolved  
373 data and a flux profile. Finally we discuss the effects of large particles not following  
374 streamlines.

##### 375 **4.1. Size Resolved Fluxes**

376 The size resolved nature of the measured dust concentrations enables derivation of size  
377 resolved dust fluxes for the flight legs where signal to noise was highest. This was the case  
378 for 18 sections of flights B600, B601, B602 and B610. The set of instrumentation, uniquely  
379 used to measure dust onboard the FAAM BAe 146, has enabled dust fluxes to be derived  
380 over a size range more than an order of magnitude wider than previous published datasets.  
381 Analyses of the size distributions themselves are presented by *Ryder et al.* [2013b]. Unique in  
382 this case was the use of an OAP for measuring dust particles and some example images  
383 showing the largest measured particles are presented in Figure 4.

384 *Kok's* [2011a] brittle fracture theory predicts that the measured flux as a function of size is  
385 controlled by cracks which split and merge during excavation of soil by saltator impacts.

$$386 \frac{dF_n(d)}{d \log(d)} \propto d^{-2} \left\{ 1 + \operatorname{erf} \left[ \frac{\ln(d/d_s)}{2 \ln(\sigma_s)} \right] \right\} \exp[-(d/\lambda)^3] \quad (5)$$

387 where  $F_n(d)$  is the size resolved number flux,  $d$  is particle diameter,  $\lambda$  is the scale length  
388 representing the penetration distance of secondary cracks and  $d_s$  and  $\sigma_s$  are the geometric  
389 mean and standard deviation of the soil particle size distribution. Transformation of (5) can

390 easily be performed to give a similar function for the size resolved mass flux,  $F_m$ . (5) is the  
391 product of a power law, a soil function and a scaling function. The power law is predicted by  
392 brittle fracture theory. The soil function represents the indivisible nature of the fully dispersed  
393 soil and causes a reduction in flux at small sizes. *Kok* [2011a] suggested that a single set of  
394 values for the two soil parameters ( $d_s=3.4 \mu\text{m}$ ,  $\sigma_s=3.0$ ) is consistent with all available dust  
395 flux data. The scaling function is chosen to be of a functional form which fits the data;  
396 generally an exponential is used [*Åström*, 2006]. The scale length used by *Kok* [2011a] was  
397  $12 \mu\text{m}$ , which was empirically derived by fitting to available flux data. The scale length and  
398 soil parameters used by *Kok* [2011a] provided a flux distribution which followed a power law  
399 in the diameter range  $2\text{-}10 \mu\text{m}$  with lower fluxes for smaller and larger diameters. *Kok*  
400 [2011a] stated that all existing size resolved flux data were compatible with a single set of  
401 values for  $\lambda$ ,  $d_s$  and  $\sigma_s$ .

402 When comparing our results to (5) we group data according to properties which may  
403 influence the flux. In one case we group data by terrain type to test for differences in the soil  
404 parameters and in another case we group data according to vertical turbulent kinetic energy  
405 ( $\text{VKE}) = \overline{w'^2} / 2$  to test for transport effects. We do not attempt to group by wind speed as we  
406 have no way to determine surface wind speeds from our measurements at altitude. The  
407 grouped size resolved fluxes, normalized over the  $2\text{-}10 \mu\text{m}$  range, are presented in Figure 5.  
408 Also shown on Figure 5 is (5) using the original *Kok* [2011a] parameters and (5) fitted to the  
409 datasets using  $d_s$ ,  $\sigma_s$  and  $\lambda$  as free parameters.

410 The aircraft data near the centre of the distributions fit within their spread to the  $-2$  power law  
411 predicted by (5). Because the measurements were made at  $60\text{--}800 \text{ m}$  altitude this result  
412 indicates that processes such as advection or vertical transport have not modified the shape of  
413 the flux distribution for these sizes. The original parameterization fits the data well over the  
414  $2\text{-}10 \mu\text{m}$  diameter normalization range where *Kok* [2011a] suggested the flux should follow a  
415 power law. However the large particle size cut-off at  $\sim 20 \mu\text{m}$  in the parameterization is not  
416 seen in the observations. The extension of the power law beyond  $20 \mu\text{m}$  is somewhat  
417 surprising given that particles larger than this diameter can be lifted directly by aerodynamic  
418 forces or particle splash [*Kok et al.*, 2012]. Hence we might not expect the brittle  
419 fragmentation mechanism to correctly predict the size resolved flux of loose particles above  
420 this size. If, however, these particles are aggregates made of material which was bound  
421 within the soil, then we would expect the brittle fracture mechanism to apply. The scale

422 invariance of the brittle fracture mechanism predicts that large aggregates will be created  
423 provided that the scaling parameter is sufficiently large. The images presented in Figure 4  
424 show at least one particle which can be identified as a large aggregate despite the 15  $\mu\text{m}$   
425 resolution.

426 At the small sizes we again see an extension of the power law beyond the original  
427 parameterization. Best fit values for the soil parameters which control the curve at small sizes  
428 are given in Table 2. In all cases the geometric mode is significantly smaller than that given  
429 in the original parameterization of  $3.4 \pm 1.9 \mu\text{m}$ . We also see differences between the different  
430 emission locations. Dune covered terrain provides the lowest relative flux of small particles  
431 and the crusted terrain provides the highest relative flux of small particles. The dust flux over  
432 Regueibat is fitted by the smallest values of the soil parameters, whereas that over the El  
433 Djouf Basin dunes is fitted by the highest values of the soil parameters. These variations are  
434 consistent with the expectation that crusted terrain consists of a fine soil particles giving  
435 stronger cohesive forces and that dunes consist of coarse soil particles giving low cohesion.  
436 The impact of these differences is that the dust flux over the crusted surface of Regueibat  
437 follows a power law to smaller diameters than over El Djouf Basin dunes. The different VKE  
438 ranges show less variability for small particles than the different terrain categories and there  
439 is no clear correlation between the best fit soil parameters and VKE as can be seen in Table 3.  
440 The results of *Sow et al.* [2009] show some deviations from our result similar to those of the  
441 [*Kok, 2011a*] parameterization. This is not surprising given that this data set was use in the  
442 tuning of the parameterization. We note however, that the *Sow et al.* [2009] data shows an  
443 increased flux at its smallest size. This data point is in better agreement with the  
444 measurements presented here than the four points which follow.

445 The large particles, from 5  $\mu\text{m}$  up to 300  $\mu\text{m}$  dominate the mass flux, contributing 90 %.  
446 They are ubiquitous in the flux measurements and are not limited to the higher dust loading  
447 events. They include particles that would usually be categorized as saltators and not be  
448 expected to leave the saltation layer within a few cm of the surface. Although cohesive forces  
449 are low for large particles and they can be emitted via direct aerodynamic uplift or via a  
450 splash mechanism [*Kok et al., 2012*], we see in Figure 5 that the flux distribution for these  
451 large particles can be effectively modeled by the brittle fracture parameterization if  $\lambda$  is  
452 increased sufficiently. Because of poor counting statistics at the larger sizes the uncertainties  
453 are large. However the curves for the highest VKE in Figure 5a and b extend to larger

454 diameters than the curves for lower VKE. This indicates an influence of vertical transport  
455 upon the maximum particle size for which a positive flux occurs. Figure 6 shows how  $\lambda$   
456 varies for the three different VKE categories. A clear correlation is seen, consistent with the  
457 hypothesis that VKE affects the particle size range over which the dust flux occurs. It is not  
458 sufficient, however, to prove a causal link. VKE could, for example, be correlated with peak  
459 horizontal winds and hence saltator impact velocities. However, the impact of wind speed  
460 upon size distribution is disputed [Alfaro *et al.*, 1997; Kok, 2011b]. If, however, VKE is  
461 regulating the flux through transport then the physical interpretation of  $\lambda$  shifts from being  
462 related to the brittle fracture process itself to being a limit imposed by the dynamics of  
463 vertical mixing. This would mean that the maximum diameter of dust emitted into the  
464 boundary layer is limited by vertical transport and is independent of the emission mechanism.  
465 It is not surprising that the exponential cut-off term in (5) can describe both processes, as it is  
466 often used as a proxy for a number of particle size limiting processes in brittle fracture  
467 parameterizations [Åström, 2006].

468 To date no other studies have observed fluxes of such large particles and we suggest some  
469 hypotheses here to explain this discrepancy. The first possibility is measurement bias. Large  
470 aerosol particles are difficult to measure because they are found in low concentrations and  
471 tend to be lost to gravitational settling and inertial impaction inside instrument inlets and  
472 pipes. Sow *et al* [2009] reported a cut-off diameter of 40  $\mu\text{m}$  for their sampling system and  
473 reported size resolved data up to diameters of 15  $\mu\text{m}$ . Detections of larger particles were too  
474 infrequent for use. Gillette *et al.* [1972] collected particles on a silicone oil covered slide and  
475 reported results up to 12  $\mu\text{m}$  diameter. By comparison the FAAM BAe 146 is equipped with  
476 open path instrumentation for particles above 3  $\mu\text{m}$  diameter, so avoid sampling system  
477 losses. This ensures that the maximum measured diameters are limited only by the scarcity of  
478 large particles. A second explanation could be that the large mass and terminal velocity of  
479 these particles makes it difficult for them to be lifted out of the saltation layer. So close to the  
480 surface turbulent eddies are limited in their scale so cannot generate the  $\sim 0.1\text{-}2.0\text{ m s}^{-1}$   
481 vertical wind velocities needed to suspend these particles. However upslope winds can  
482 generate vertical velocities of this magnitude and flow separation at slope peaks can inject the  
483 particles to heights of 10s or 100s of meters. Once at these heights the intense turbulence  
484 generated over the Sahara can mix the particles throughout the boundary layer. At 100 m  
485 above the Saharan surface the aircraft typically measured  $\pm 4\text{ m s}^{-1}$  peak vertical wind speeds.  
486 The slopes involved could be hill and valley systems [Egan, 1984] such as those found at El



487 Hank or dunes [*Schatz and Herrmann, 2006*] such as found in Erg Chech. The tendency to  
488 mount instrumentation away from such features to avoid contamination of results [*Gillette et*  
489 *al., 1974; Sow et al., 2009*] will have resulted in such an injection mechanism being missed.

490 The impact of these large dust particles is restricted to the local region. They have terminal  
491 velocities of the order  $1 \text{ m s}^{-1}$  and hence even when mixed to 5 km altitude they will settle to  
492 the surface overnight, although shear driven turbulence or lifting from haboobs are able to  
493 keep large particles aloft longer [*Ryder et al., 2013a*]. Despite the fast settling, large particles  
494 may have a significant local impact on air quality, visibility, radiative balance, and cloud  
495 processes. Because the dust is so large it will act as cloud condensation nuclei (CCN)  
496 [*Koehler et al., 2009*] and even as a Giant CCN. If uplift of such large dust particles is found  
497 to exist beyond just the Sahara, then other large human populations will be affected. There  
498 will be an impact upon estimates of increased melt rate of glaciers and seasonal snow packs  
499 due to dust deposition which has both distant [*Sodemann et al., 2006; Painter et al., 2007*]  
500 and local moraine [*Oerlemans et al., 2009*] sources. There will also be an impact upon  
501 estimates of uplift from soils containing volcanic material, for example in Iceland [*Stuart,*  
502 *1927; Arnalds et al., 2001*] (i.e. resuspended volcanic ash) where aircraft and surface  
503 observations have shown significant uplift [*Blechs Schmidt et al., 2012; Prospero et al., 2012*].  
504 Such uplifted dust is likely to present a similar aviation hazard to volcanic ash [e.g. *Prata and*  
505 *Tupper, 2009; Drexler et al., 2011*].

#### 506 **4.2. Flux source and drift velocity**

507 Although surface emission is the initial source of dust, once it has been lifted other non-  
508 emission processes may affect the flux, including, particle settling, entrainment and  
509 differential advection. Particle settling causes particles to become concentrated in the lower  
510 atmosphere and generates a concentration gradient. Vertical mixing across this gradient  
511 generates a flux which counters the gravitational settling. Entrainment at the boundary layer  
512 top generates a flux because the air above the boundary layer generally contains a different  
513 (usually lower) concentration of dust to the boundary layer itself. Boundary layer growth and  
514 entrainment generates a concentration gradient and mixing across this again generates a flux.  
515 Finally differential advection can bring together air from different source regions at different  
516 altitudes, this air may have different dust concentrations and again mixing across this  
517 concentration gradient generates a flux. We mostly expect that flux due to differential

518 advection will be low, because the boundary layer is well mixed and above the surface layer  
519 we expect the wind to be approximately constant.

520 It is possible to distinguish between fluxes generated by emission and these other  
521 mechanisms by considering the drift velocity of the dust (also referred to as emission velocity  
522 for direct measurements of emission [Dorsey *et al.*, 2002]). Drift velocity is given by  $v_d(d) =$   
523  $F_n(d) / n(d)$  and the relationship between  $v_d(d)$  and the gravitational settling velocity,  $v_s(d)$ , is  
524 different for each case. In the case where we have a flux generated only by gravitational  
525 settling we expect to see either a balanced system where  $v_d \approx -v_s$ , or an unbalanced system  
526 where previous emission has not yet reach equilibrium and hence  $v_d < -v_s$ . These comparisons  
527 apply for all diameters. Where we have a flux due to entrainment of clean air  $v_d$  is larger than  
528  $v_s$  and as the concentration of particles becomes diluted  $v_d$  increases further and hence we  
529 expect  $v_d \geq -v_s$  for all diameters. The increase in  $v_d$  should be particularly large for large  
530 particles which are particularly scarce above the boundary layer. For flux due to differential  
531 advection we expect no particular relationship between  $v_d$  and  $v_s$  and may find that  $v_d$  is  
532 negative. Finally, for emission  $v_d$  is initially larger than  $v_s$ . However, as the concentration of  
533 particles increases,  $v_d$  decreases until the atmosphere saturates for a given particle diameter,  
534 giving  $v_d \approx -v_s$ . Because the magnitude of  $v_s$  increases with  $d^2$  and because (5) predicts that  
535 for particles larger than 1  $\mu\text{m}$  flux decreases as  $d^2$  or faster, we expect that large particles will  
536 reach a balance with gravity much sooner than small particles. Hence for emission we should  
537 find that a saturation diameter,  $d_{sat}$ , exists such that  $v_d(d) > -v_s(d)$  for  $d < d_{sat}$  and  $v_d(d) \approx -$   
538  $v_s(d)$  for  $d > d_{sat}$ .

539 Figure 7 shows measured drift velocities and calculated settling velocities as a function of  
540 diameter for the peak flux measurements of flights B600, B602 and B610. Settling velocities  
541 were derived assuming standard surface conditions for deriving atmospheric density and  
542 viscosity. Settling velocities deviate from a power law at large sizes due to the transition to  
543 turbulent flow around the particles, which are assumed to be spherical. We see that smaller  
544 particles have  $v_d \gg -v_s$  and for larger particles  $v_d \approx -v_s$ . This is consistent only with the recent  
545 local uplift scenario, it is not consistent with balancing of flux with gravitational settling of  
546 particles having undergone long range transport, nor with entrainment of clean air at the  
547 boundary layer top. Although we cannot absolutely rule out that the flux is due to differential  
548 advection, it seems highly unlikely that in all three of these cases the same pattern would be  
549 generated by this mechanism. Of course some horizontal transport of the measured particles

550 must have occurred, as they require a finite time to mix up to the altitude of the aircraft.  
551 However, this analysis indicates that the transport time is significantly smaller than the time  
552 required to mix emission through the boundary layer. The strong updrafts of a few  $\text{m s}^{-1}$   
553 measured in the boundary layer would be expected to perform such mixing on time scales of  
554 the order one hour, leading to the conclusion that emission must have occurred within a few  
555 tens of km of the measurement location.

### 556 **4.3. Total Number Fluxes and Mass Fluxes**

#### 557 **4.3.1. B600, B601, B602 Broad Harmattan LLJ**

558 Figure 8 shows measured surface and atmospheric parameters as well as the number and  
559 mass fluxes derived for the three broad scale Harmattan LLJ flights, B600, B601 and B602.  
560 To the south, where the LLJ was forecast to be strongest, the dust number and mass  
561 concentrations tended to be the highest. The B600 and B602 flights occurred in the morning  
562 closer to the expected time of LLJ breakdown. In these cases highly variable regions of dust  
563 concentration were associated with peak dust fluxes towards the south of the legs and nearest  
564 to the forecast LLJ position. Further north the dust concentration was lower and less variable,  
565 but with a few spikes in concentration which may represent small uplift events. These two  
566 flights also showed the largest dust fluxes which peaked to the south, with values of  
567  $(1.2 \pm 0.40) \times 10^7 \text{ m}^{-2} \text{ s}^{-1}$  and  $0.37 \pm 0.18 \text{ mg m}^{-2} \text{ s}^{-1}$  for B600 and  $(1.6 \pm 0.17) \times 10^7 \text{ m}^{-2} \text{ s}^{-1}$  and  
568  $0.20 \pm 0.051 \text{ mg m}^{-2} \text{ s}^{-1}$  for B602. The uncertainty of the B600 peak is large because quickly  
569 varying conditions along the flight track limited the integration time to only 300 s, compared  
570 to 700 s for the B602 peak. The B600 and B602 flux maxima were recorded at the southern  
571 and northern perimeter of the El Djouf Basin. Both locations consist of dune terrain and both  
572 provide rapid changes in topography of 10s of meters. A second peak of flux was observed  
573 over the El Hank region at  $23.7^\circ \text{ N}$ . Here again large elevation changes were observed in the  
574 surface topography and the wadis provide a supply of easily erodible material. There is  
575 clearly not a one-to-one correspondence between measured wind speeds and measured fluxes.  
576 This is to be expected given the altitude at which the measurements are taken and that the  
577 emission which led to our flux measurements is dependent upon surface properties as well as  
578 wind speed. However all significant fluxes during B600 and B602 occurred in regions where  
579 wind speed was above average for the flight. The El Hank region is on the periphery of the jet  
580 and it is perhaps surprising to see emission from here, albeit with lower fluxes than to the  
581 south. At El Hank the measured wind speeds were  $< 10 \text{ m s}^{-1}$  but to the south were  $> 15 \text{ m s}^{-1}$ .

582 This region has a much lower albedo than its surroundings and correspondingly higher  
583 surface temperatures which must have decreased stability and increased mixing down of  
584 momentum [Marshall *et al.*, 2008; Huang *et al.*, 2010]. The complex terrain will also funnel  
585 winds. These factors favor dust emission in this region. This may also mean that at the flight  
586 time the mixing of momentum was more advanced and that the winds had passed their peak.

587 The afternoon B601 flight after LLJ breakdown was much calmer by comparison. The dust  
588 concentration was lower and less variable. This flight shows little flux for all regions and the  
589 wind speeds had dropped to  $\sim 12.5 \text{ m s}^{-1}$  at the aircraft altitude. The forecast surface speeds  
590 seen in Figure 2 were also much lower. The only small but significant rise above zero flux  
591 was observed at  $21.8^\circ \text{ N}$ . This coincides with a dry channel which appears to have once  
592 drained from a small basin covering  $\sim 500 \text{ km}^2$  to the NE. Such a region is likely to contain  
593 fluvial deposits available for uplift and also has varying topography. Despite the low flux  
594 observed, SEVIRI data in Figure 2 shows the most intense pink dust color at this time. This  
595 dust must be previously uplifted, and then mixed up to altitudes where it is more easily  
596 identified in SEVIRI imagery.

597 The peak number fluxes measured during B600 and B602 are of a similar order of magnitude  
598 to those of Sow *et al.* [2009], which covered a range of approximately  $(0.5-5) \times 10^7 \text{ m}^{-2} \text{ s}^{-1}$  for  
599 two monsoon emission events and one convective event. We observed peak values of  
600  $dF_n/d\log(d)$  of  $(1-2) \times 10^7 \text{ m}^{-2} \text{ s}^{-1}$  for particles with diameters less than  $1 \mu\text{m}$ . This is within the  
601 range of approximately  $(0.6-10) \times 10^7 \text{ m}^{-2} \text{ s}^{-1}$  observed in a similar size range by Sow *et al.*  
602 [2009]. These values are also similar or slightly higher than those presented by Gillette *et al.*  
603 [1972]. The peak mass fluxes are also within the range measured using a TEOM mass  
604 balance by Sow *et al.* [2009], giving results which varied from approximately 0.1 to several  
605  $\text{mg m}^{-2} \text{ s}^{-1}$ .

606 During the B600 and B601 flights there was a large plume of material seen to extend from  
607 Algeria over Mali and Mauritania on SEVIRI satellite imagery. It is not immediately clear  
608 how much of the dust was transported compared to that which was locally uplifted. However,  
609 the largest observed fluxes are clearly linked to this plume. For flight B602, however, there  
610 are more local enhancements in dust seen on SEVIRI imagery, allowing us to qualitatively  
611 validate the locations of emission by examining the evolution of SEVIRI imagery. Figure 9  
612 shows a comparison of two SEVIRI images from the morning and afternoon of 18<sup>th</sup> June  
613 2012, before and after the measurements made by flight B602. It is clear that over the

614 intervening time, two isolated pink regions developed in the region over which the  
615 measurements were made. The first is a stripe down the approximate centre of El Hank and  
616 the second is in a region which follows the Hamada Safia ridge on the northern edge of the  
617 El Djouf Basin. These two locations correspond to the two B602 peaks observed in Figure 8  
618 at 22.8 and 23.3° N and this correspondence provides good qualitative support of the results.  
619 The SEVIRI detection of dust reaches its peak after the flight because the dust increases in  
620 contrast as it accumulates in the boundary layer and as it is mixed upwards.

621 The ogives presented in Figure 10 show the eddy scales that contributed to the fluxes. For  
622 B600 some ogives do not flatten at large wavelengths despite legs of up to 100 km. Such  
623 large length scales indicate some contribution of processes other than simple boundary layer  
624 turbulence and highlights the difficulty in balancing sufficient counting statistics, covering  
625 the lengths scales involved and maintaining homogeneity. The ogives for B602 are well  
626 bounded and show contributions from wavelengths of 0.1 to 5 km. This range reflects the fact  
627 that the Saharan boundary layer can exceed 5 km in depth. We found that vertical wind  
628 spectra follow the Kolmogorov  $-5/3$  power law for eddy length scales between 30 and 400 m.  
629 For flight B601 in the late afternoon the length scales are similar to those of B602. It is of  
630 some note that even for model runs covering large areas of North Africa, grid-spacings of  
631 below 5km have been used [*Marsham et al.*, 2011]. When length scales relevant to turbulent  
632 fluxes begin to be resolved there are potential issues with related parameterizations. For  
633 example gustiness may become resolved which would impact dust uplift schemes, boundary  
634 layer eddies would become resolved impacting transport schemes and if similar scales are  
635 important for heat and momentum flux then there may be effects related to parameterizations  
636 for these properties [e.g. *Wyngaard*, 2004; *Shin and Hong*, 2013].

637 In all of these cases the length scales associated with the flux are greater than approximately  
638 0.1 km. Large eddies of this scale are potentially organized features such as rolls or dry  
639 convective cells. Such organized structures can include large updraft speeds in the mid  
640 boundary layer and will therefore enable efficient mixing of even very large particles through  
641 the boundary layer depth. *Shpund et al.* [2011] simulated the impact of large eddies upon sea  
642 spray and moisture. They showed that the large eddies cause large particles to be mixed to  
643 greater heights in the boundary layer, reduced the gradients of aerosols and droplets and  
644 reduced the gradient of the humidity profile. Here we confirm that these large eddy scales  
645 dominate the particle flux at the heights measured.

646 **4.3.2. B610 El Hank LLJ**

647 Figure 11 shows measured values for flight B610, analogous to those discussed for flights  
648 B600-B602. El Hank is clearly defined by its rugged terrain, its low albedo and a positive  
649 surface temperature anomaly of up to 10 K. The dust concentration shows a large amount of  
650 variability, with narrow peaks across and just north of El Hank and a broader peak to the  
651 north over a valley in Regueibat Rise. As this flight was early in the morning we expected a  
652 shallower convective boundary layer and smaller eddy scales. Each leg is therefore divided  
653 into 240 s (~29 km) sections over which the flux was derived. The ogives in Figure 12 show  
654 that we have covered all contributing length scales with this integration period and indicate it  
655 could be reduced further. Doing so, however, increases the uncertainty in the measurements  
656 so gives no real benefit. Two peaks are seen in the fluxes, at latitudes of 23.5° N and on the  
657 earlier southward leg at 25° N. The more northerly peak corresponds to the concentration  
658 peak above the valley in the Regueibat Rise region where we expect an erodible source of  
659 sediments. This peak also corresponds to the highest horizontal wind speeds measured on the  
660 legs of 16 m s<sup>-1</sup>. The small positive surface temperature anomaly in this region may have  
661 helped to mix momentum down from the jet. The southern peak was over a valley and ridge  
662 of El Hank. Again here we expect to find an ample supply of erodible material, preferential  
663 mixing of the LLJ momentum due to the positive surface temperature anomaly and funneling  
664 of winds.

665 On the northward second leg the dust number flux was reduced over El Hank and had  
666 dropped to near zero over Regueibat Rise, although the mass flux over El Hank remained at  
667 its previous levels. Although there is scope for significant variation within the uncertainty,  
668 this indicates a change in the ratio of large and small particle fluxes. The VKE over El Hank  
669 was also found to increase between the first and second legs on B610 by between 12 and 34  
670 %. As discussed in 4.1 the change in VKE may be linked to the change in the sizes which  
671 contribute to the fluxes. Other possibilities which cannot be verified or discounted by this  
672 analysis could include changes in the soil characteristics, perhaps as fine soil was initially  
673 eroded exposing coarser soil beneath, or a change in the emission footprint or transport  
674 distances of the dust contributing to the flux.

675 The ogives for the flux measurements are given in Figure 12. They show that for the first leg  
676 from approximately 09:14 to 09:45 UTC the important length scales were between 0.1 and  
677 1.0 km. On the reciprocal leg between 09:50 and 10:40 the ogives were more variable and

678 some extended to length scales of 1.2 km. Presumably heterogeneous heating of the surface  
679 and boundary layer growth contributed to the variable increase in length scales. Again these  
680 scales are typical of large scale organized convection as discussed for the broad Harmattan  
681 LLJ case.

### 682 **4.3.3. B613 Flux Profile**

683 The variation of flux with altitude is expected to be defined by the conditions at the top and  
684 bottom of the boundary layer which are a function of dynamics and dust uplift. The surface  
685 boundary condition is set by the emission or deposition at this location. The upper boundary  
686 is set by the growth rate of the boundary layer and the difference in concentration between  
687 the boundary layer and the residual layer or free troposphere above. Between the two  
688 boundary conditions we might expect a linear profile of flux with altitude, similar to that  
689 observed in other tracers with surface sources such as water vapor [Stull, 1988]. This  
690 expectation is true of the small particles which dominate the number flux. The flux profile of  
691 larger particles may be more complex if they do not follow streamlines. Flight B613 involved  
692 multiple legs in the Regueibat region. The flight track incorporated mostly crusted terrain  
693 although a depression near the centre of the track contained brighter dune material with  
694 consequently cooler surface temperatures. Figure 13 shows the number concentration  
695 measured on the profile descent through the boundary layer made when the aircraft entered  
696 the area of interest and flux measurements derived from horizontal legs subsequently  
697 completed moving back up through the boundary layer. The flux profile is consistent with the  
698 linear relationship that is expected. All ogives flatten at both ends indicating we have covered  
699 all length scales. The boundary layer top can be seen from the number concentration data at  
700 4.5 km. The 0.5 km depth over which the dust concentration decreases is the entrainment  
701 zone where clean tropospheric air is being mixed into the boundary layer. In this case the  
702 boundary layer is growing slowly in the late afternoon resulting in a near zero flux at the  
703 boundary layer top. A moderate flux is observed at 400 m above the surface. Because only a  
704 moderate flux was observed the uncertainty for fluxes of particles with diameters greater than  
705 1  $\mu\text{m}$  was generally greater than 100 %. For this reason it has not been possible to use the  
706 drift velocity analysis to examine the link to the surface. We found that the small particles all  
707 have drift velocities much larger than the settling velocity, indicating that the flux is not  
708 simply mixing of particles that have undergone long range transport. The negative gradient of  
709 the flux profile indicates that the flux cannot be caused by entrainment of clean air at the

710 boundary layer top. Two remaining hypotheses are possible. The first is that the gustiness  
711 observed in the wind profile in Figure 3d has generated moderate emission. The second is  
712 that the change in wind speed with height seen in Figure 3d has caused advection of dust  
713 from different regions at different heights. This could cause a vertical concentration gradient  
714 and hence a flux. In this case it is difficult to tell which is the most likely scenario.

715 Under the assumption that the flux is caused by surface emission, extrapolation of the linear  
716 fit across the small distance to the surface results in an estimated surface emission of  
717  $(9.3 \pm 1.8) \times 10^5 \text{ m}^{-2} \text{ s}^{-1}$ . Surface fluxes cannot be derived for other flights as flux profiles were  
718 not available.

#### 719 **4.4. Impact of neglecting particle inertia**

720 As discussed previously, particle inertia causes deviation of particles from streamlines and  
721 they do not immediately respond to changes in the turbulent wind field. Equation (4) provides  
722 a correction factor which may be applied to account for these deviations. The minimum eddy-  
723 particle interaction parameter observed is 100, based upon a minimum contributing eddy  
724 scale of 0.1 km, the largest velocities of  $5 \text{ m s}^{-1}$  and the largest relaxation times of 0.2 s for a  
725  $300 \text{ }\mu\text{m}$  particle. This provides a minimum inertial correction factor very close to 1. The  
726 impact of inertia is therefore much lower than other uncertainties and has been neglected.

727 It is interesting to consider the impact of particles not following streamlines upon the actual  
728 flux as well as upon the measurements. Although at the altitude at which the measurements  
729 were made we expect even the largest particles measured to follow streamlines, this may not  
730 be the case everywhere in the boundary layer or for even bigger particles. Near the surface  
731 the eddy scales are smaller and hence streamlines have a higher. These kinds of variations in  
732 particle and atmospheric properties cause changes in  $R$  and therefore some or all layers of the  
733 atmosphere will provide very low turbulent diffusivity for particles above a threshold  
734 diameter. Gravitational settling may make these layers impassible. This provides a possible  
735 framework for examining how the height at which particles are injected into the atmosphere  
736 can affect the maximum size of particles which are mixed through the boundary layer and  
737 hence the value of  $\lambda$  derived in this work. The measurements made here are not sufficient to  
738 test such a model; modeling of the surface layer may provide some insights. Based upon this  
739 framework, however, we expect that the flux of large particles and estimates for  $\lambda$  could only  
740 increase for measurements at lower altitudes.



741 **5. Conclusions**

742 The first measurements of size resolved dust fluxes from an aircraft and the first dust flux  
743 measurements from the heart of the Sahara are presented. The benefits of the aircraft platform  
744 include an ability to access remote areas, cover multiple regions with different surface  
745 properties affecting dust uplift and the ability to target features of meteorological interest.  
746 One particular difficulty is the speed at which the aircraft travels, which impacts its ability to  
747 get good counting statistics within a heterogeneous region and measure small scale  
748 turbulence. The other important difficulty is the limit on the lowest altitude at which the  
749 measurements can be made, which is dependent upon visibility and affects the ability to link  
750 measured fluxes to surface emission without flux profiles being taken. Careful calibration of  
751 the instruments and appropriate refractive index corrections of the optical particle counters  
752 have ensured that continuous distributions of size-resolved particle fluxes have been possible  
753 from ~0.1-300  $\mu\text{m}$  diameter, with the upper size only limited by the scarcity of large  
754 particles. This size range is more than an order of magnitude larger than has been achieved in  
755 previous studies. The methods used have been shown to be robust with ogives indicating that  
756 all turbulent scales are captured and with emission locations consistent with SEVIRI satellite  
757 observations. Analysis of the size dependant particle drift velocity and comparison with the  
758 particle settling velocity provided validation that measured flux was linked to recent local  
759 emission. Positive validation was provided for the three cases closest in time and space to  
760 breakdown of a low level jet. The remaining two cases, including a flux profile, had lower or  
761 near zero fluxes and the number flux of large particles was not great enough to indicate  
762 whether the flux in this case was due to local emission. The methods used here are not  
763 necessarily limited to dust; particle fluxes of other aerosol types could be measured by the  
764 instrument suite on board the FAAM BAe 146 aircraft.

765 The large measurement range has allowed us to show that the mode in the dust mass flux is at  
766 diameters of 30-100  $\mu\text{m}$  and these large particles provide approximately 90 % of the mass  
767 flux. This was observed in moderately dusty conditions and in high dust concentrations, i.e. it  
768 was a ubiquitous feature of the emission not confined to large events. The largest of these  
769 particles would usually be regarded as saltators and not be expected to be lifted above a few  
770 cm from the surface. We hypothesize that these particles may be injected to 10s or 100s of  
771 meters above the surface by flow separation at ridges, cliffs or sand dunes. Once at this height  
772 the intense turbulence above the Sahara with typical vertical velocities of  $\pm 4 \text{ m s}^{-1}$ , even at

773 100 m above the surface, is able to suspend these particles and mix them throughout the  
774 boundary layer.

775 The *Kok* [2011a] model of brittle fracture was able to represent the flux size distribution for  
776 particles with diameters between 1 and 20  $\mu\text{m}$ . This parameterization predicts a power law  
777 distribution with deviations controlled by the geometric mean diameter and standard  
778 deviation of the emitting soil,  $d_s$  and  $\sigma_s$ , and an empirical scale parameter,  $\lambda$  which causes  
779 drop off at large diameters. The power law distribution in our measurements extended to  
780 much larger sizes than suggested by *Kok* [2011a] with values of  $\lambda$  of 43 – 144  $\mu\text{m}$  compared  
781 to the *Kok* [2011a] suggested value of 12  $\mu\text{m}$ . The best fit value of  $\lambda$  correlated well with  
782 atmospheric VKE indicating that  $\lambda$  may represent a cut off controlled by atmospheric  
783 turbulent transport rather than the emission process itself. Although this interpretation of  $\lambda$  is  
784 due to a completely different mechanism to that suggested by brittle fracture theory, the  
785 empirical nature of the scale parameter and scaling function means it is unsurprising that the  
786 same functional form fits this data. Another possible explanation for the correlation of  $\lambda$  with  
787 VKE would be a correlation of VKE with another atmospheric parameter (e.g. near surface  
788 wind speed) which could affect the emission process directly, although such correlations are  
789 not well constrained [*Alfaro et al.*, 1997; *Kok*, 2011b]. The scale of turbulence was also  
790 shown to affect the flux and measurement of flux when turbulent scales are small and air  
791 motion is fast, because large particles are not able to follow the streamlines. It was shown that  
792 for the measured conditions the impact was negligible, however this mechanism may  
793 contribute to limiting of the maximum emitted particle diameter in other atmospheric layers.  
794 The soil related parameters were required to be much smaller than the values found by [*Kok*,  
795 2011a] in order to fit our measurements. The surface type affected the flux at small sizes with  
796 best fits of  $d_s$  and  $\sigma_s$  varying by factors of 2 and 1.5 respectively. The largest values of  $d_s$  and  
797  $\sigma_s$  were found over dunes and the smallest over stable terrain. The lack of previous  
798 measurement of fluxes of such large particles may be because of the difficulties in measuring  
799 such particles with inlet based instruments or could be because of the hypothesized  
800 dependence upon topography which is usually avoided when making flux measurements.

801 The impact of emission of such large particles will be on local scales due to their high  
802 deposition rate. However, they may still affect local radiative transport and cloud processes  
803 where they can act as (giant) cloud condensation nuclei. If large particle emission is  
804 important in regions outside the Sahara then the impact will extend to diverse fields such as

805 estimates of air quality in populated areas, aviation hazards from resuspension of volcanic ash  
806 and enhancement of glacier and snow pack melting by albedo reduction.

807 All the cases presented here were linked to nocturnal low level jet (LLJ) breakdown  
808 phenomena. However, this is a biased sample because LLJs are relatively easy to forecast and  
809 target compared to haboobs. Despite the altitude at which the measurements were made the  
810 magnitude of the number and mass fluxes presented here are consistent with or slightly larger  
811 than the size resolved number fluxes measured by *Sow et al.* [ 2009] and *Gillette et al.* [1972]  
812 and the total mass fluxes measured by *Sow et al.* [ 2009]. We found peak number fluxes,  $F_n$ ,  
813 of  $(0.7-1.6)\times 10^7 \text{ m}^{-2} \text{ s}^{-1}$ , peak mass fluxes,  $F_m$ , of  $0.20-0.37 \text{ mg m}^{-2} \text{ s}^{-1}$  and peak values of  
814  $dF_n/d\log(d)$  of  $(1-2)\times 10^7 \text{ m}^{-2} \text{ s}^{-1}$ . For each case the dust flux was found to be highly variable  
815 as a function of location. All the highest measurements of dust number flux made during  
816 Fennec occurred over regions of varying topography. Although this is consistent with the idea  
817 that flow separation is important in lifting particles out of the surface or saltation layer, this  
818 work cannot explicitly make a causal link. The correlation may instead be due to the  
819 abundance of erodible material at these sites or impacts of the terrain upon local meteorology,  
820 such as funneling of winds.

821 We found that for the relatively simple case where we had emission at the surface and slow  
822 growth of the boundary layer into a relatively clean free troposphere the flux varied linearly  
823 with altitude, as expected.

824 Ogives were used to probe the important length scales over which dust flux occurred. The  
825 important length scales for mixing of dust were found to be between 1 and 0.1 km for the  
826 earliest measurements of LLJ breakdown at approximately 09:00 UTC. Later in that same  
827 flight, around 10:00 UTC, the largest important length scales had increased slightly, to  
828 approximately 1.2 km and the ogives were more variable. In other flights later in the morning  
829 well bounded ogives covered scales up to 10 km. Some ogives did not flatten at large scales  
830 even out to 50 km, probably indicating mesoscale contamination. By late afternoon the  
831 largest important scales had reduced to 1.4 km. Given that regional research models over the  
832 Sahara have been run at 1.5 km we are entering a “gray zone” where some of this flux is  
833 resolved by the model dynamics.

834 These measurements have prompted a number of hypotheses detailed here. Testing of these  
835 hypotheses and assessing of the impact of these findings requires further modeling and

836 measurement work. Some particular challenges include testing of how flow separation affects  
837 vertical mixing of dust compared to mixing of particles (particularly large particles) from a  
838 flat saltation layer and how VKE and the eddy-particle interaction parameter affects  
839 subsequent upward transport. The global importance of such processes for large particles is  
840 linked to the transport distances of these large particles and assessment of whether emission  
841 of such large particles is ubiquitous or occurs only in the Sahara's intense dry convection.  
842 These challenges will require the use of regional, global and large eddy simulations together  
843 with observations of transported material [e.g. *Ryder et al.*, 2013a].

## 844 **6. Acknowledgements**

845 We would like to acknowledge and thank the following institutions. This work and the  
846 Fennec project were funded by the Natural Environment Research Council (NERC) grant  
847 number NE/G017166/1. Airborne data was obtained using the BAe-146-301 Atmospheric  
848 Research Aircraft flown by Directflight Ltd and managed by the Facility for Airborne  
849 Atmospheric Measurements, which is a joint entity of NERC and the Met Office. Model  
850 simulations were provided by the Met Office. SEVIRI imagery was provided by  
851 EUMETSAT and hosted by Imperial College London. Model and airborne data were hosted  
852 by the British Atmospheric Data Centre. Surface imagery courtesy of the Blue Marble Next  
853 Generation, Reto Stöckli, NASA Earth Observatory.

854 We would like to thank Jasper Kok and two other anonymous reviewers for their insightful  
855 and valuable contributions.

856

857

858 Table 1. Summary of flights for which dust fluxes have been derived

Flight Number	Date	Entered Area of Interest (UTC)	Left Area of Interest (UTC)	Altitude Range Above Surface* (m)	AOD**	Conditions	Location
B600	17/6/2011	10:10:00	11:12:35	680-800	2.24	Harmattan wind with	Regueibat Rise, El Hank, Erg
B601	17/6/2011	16:57:00	18:19:03	720-820	3.08	LLJ features breaking	Chech, El Djouf Basin
B602	18/6/2011	10:18:08	11:27:27	110-70	1.07	down during the day	
B610	25/6/2011	08:57:22	10:39:33	60-150	0.52, 1.75	Narrow LLJ	Regueibat Rise, El Hank, Erg Chech
B613	26/6/2011	15:17:47	17:31:16	70 -4300	0.55, 0.55	Stacked legs in light wind after LLJ breakdown	Regueibat Rise

859

860 \*Measured by a radar altimeter (surface referenced) for heights below 2000 m or by GPS (ellipsoid referenced) above 2000 m. Only heights  
861 where fluxes were measured are included.

862 \*\*Aerosol optical depth at 550 nm (AOD) was derived by integration of aircraft measurements during profiles between the transit altitude (~8  
863 km) to the lowest flight level. The first measurement for each flight was made as the aircraft entered the area of interest, the second value (where  
864 available) was made as the aircraft left the area of interest.

865

866 Table 2. Soil related best fit parameters for different overflown regions

Region	$d_s$ ( $\mu\text{m}$ )	$\sigma_s$ ( $\mu\text{m}$ )
El Hank	0.46±0.06	1.8±0.2
Erg Chech and El Djouf Basin (dunes)	0.78±0.2	2.5±0.3
El Djouf Basin (dune free)	0.61±0.09	2.1±0.2
Regueibat	0.38±0.05	1.6±0.2

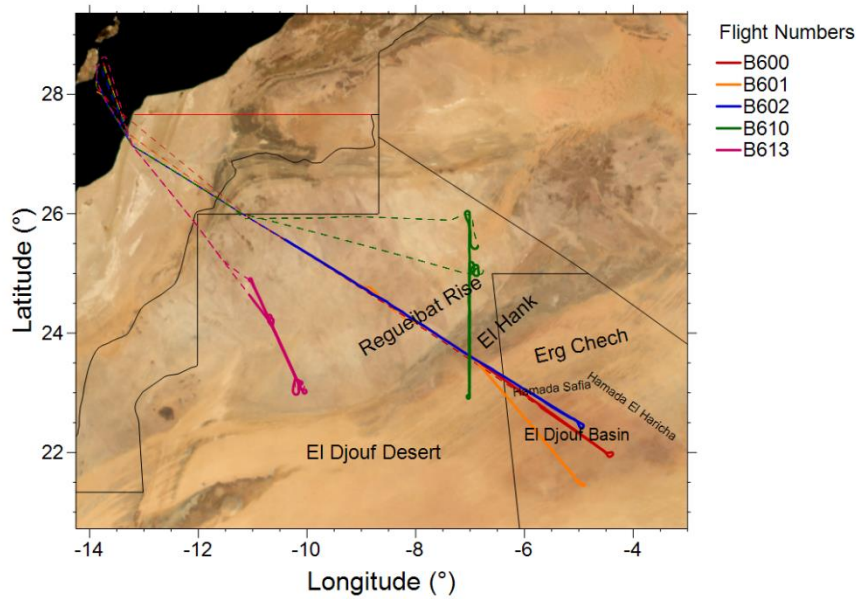
867

868

869 Table 3. Soil related best fit parameters for different values of VKE

Region	$d_s$ ( $\mu\text{m}$ )	$\sigma_s$ ( $\mu\text{m}$ )
$0.35 < \text{VKE} < 0.6$	$0.54 \pm 0.09$	$1.8 \pm 0.2$
$0.6 < \text{VKE} < 0.85$	$0.74 \pm 0.2$	$2.7 \pm 0.5$
$0.85 < \text{VKE} < 0.10$	$0.53 \pm 0.07$	$2.0 \pm 0.2$

870



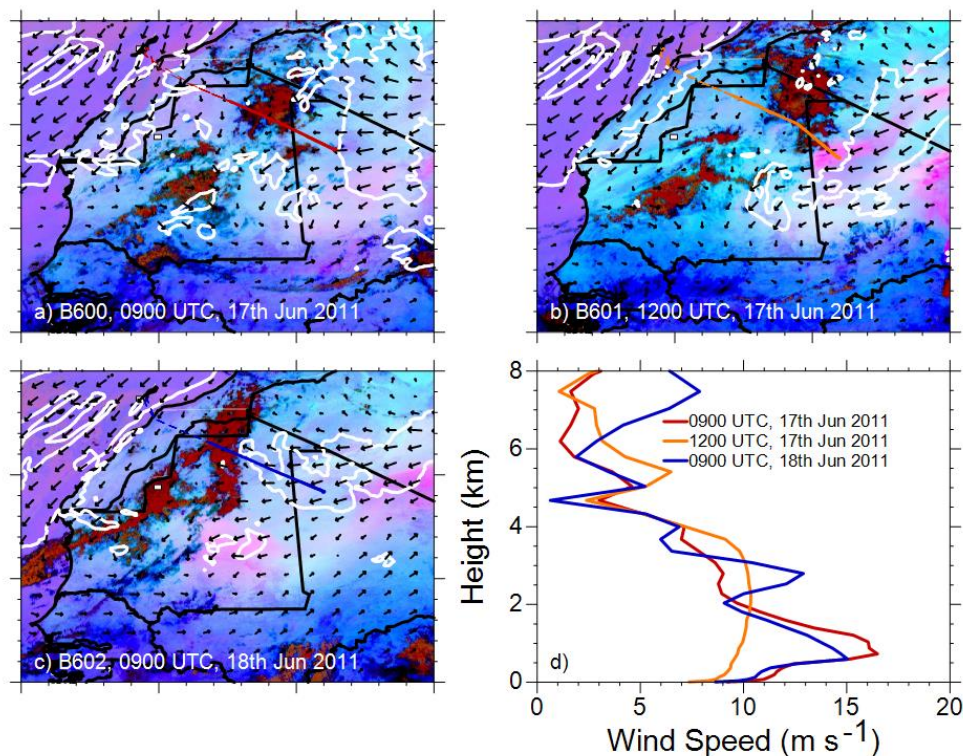
871

872 Figure 1. Aircraft tracks overlain upon cloud filtered satellite imagery [Reto *et al.*, 2005]  
873 labeled with geographical features of note. Bold lines show aircraft tracks below 6.0 km in  
874 the area of interest and fine dashed lines show tracks for higher altitude flying, takeoffs and  
875 landings. The overlain northern end-points of the low-level tracks of B600 and B601 are  
876 within 0.5 ° of the northern end-point of the visible B602 low-level track.

877



878

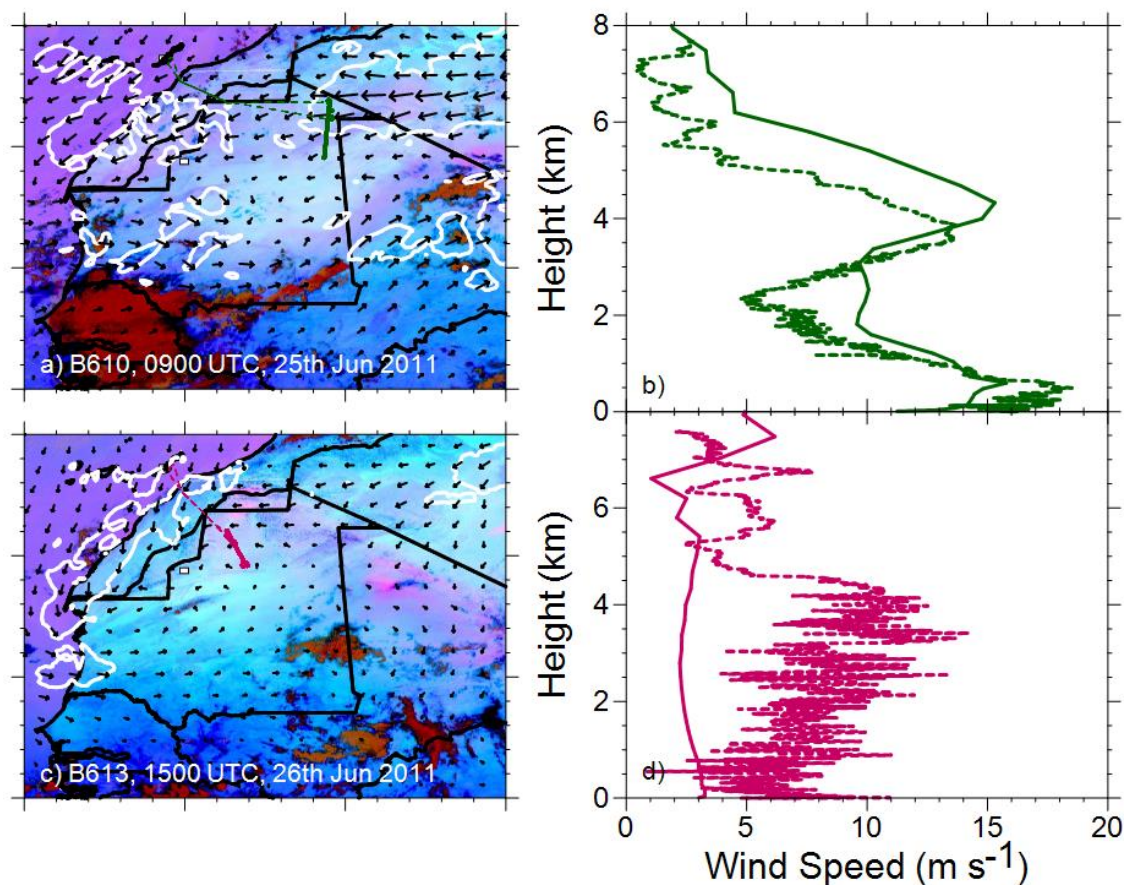


879

880 Figure 2. False color SEVIRI images for 0900 UTC (a), 1200 UTC (b) from the 17<sup>th</sup> June  
881 2011 and 0900 UTC on the 18<sup>th</sup> (c) overlain with wind vectors forecast by the Africa LAM  
882 operational model on its lowest level (10 m). The white contour is at 8.0 m s<sup>-1</sup>. Colored lines  
883 show aircraft tracks as in Figure 1. Dust is evident as a pink color and can be seen to form a  
884 band stretching from Algeria to the Mali/Mauritania border during the 17th corresponding to  
885 regions of high forecast winds. Panel (d) shows the forecast wind profiles at the most SE  
886 point of the aircraft track at the same times as panels (a)-(c).

887

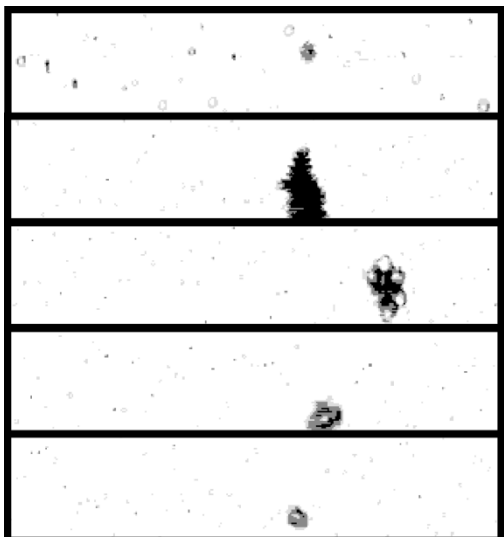
888



889

890 Figure 3. Images (a) and (c) show false color SEVIRI images overlain with forecast Africa  
891 LAM wind vectors and the white 8 m s<sup>-1</sup> contour as per Figure 2, for times corresponding to  
892 flights B610 and B613. Colored lines show aircraft tracks as for Figure 1. Images (b) and (d)  
893 show forecast Africa LAM wind profiles at the same times as (a) and (c) respectively, with  
894 corresponding measured wind profile from the aircraft descents.

895

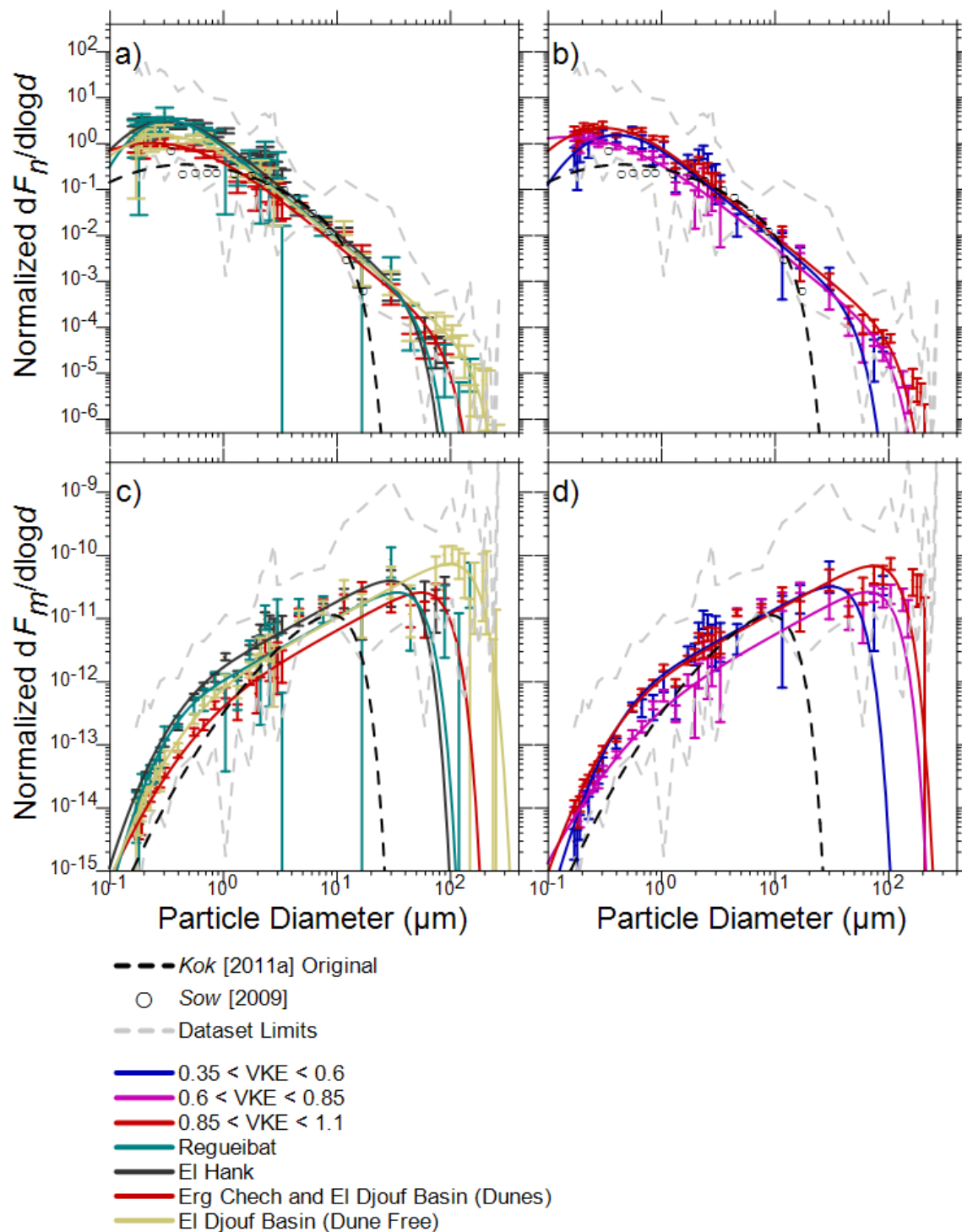


896

897 Figure 4. Example images of large dust particles collected by the CIP15 probe during flight  
898 B601. The image resolution is 15  $\mu\text{m}$  and the height of each strip is 960  $\mu\text{m}$ . Note that the  
899 CIP only records pixels when a particle is in the field of view so horizontal spacing in the  
900 images is not representative of actual particle spacing.

901

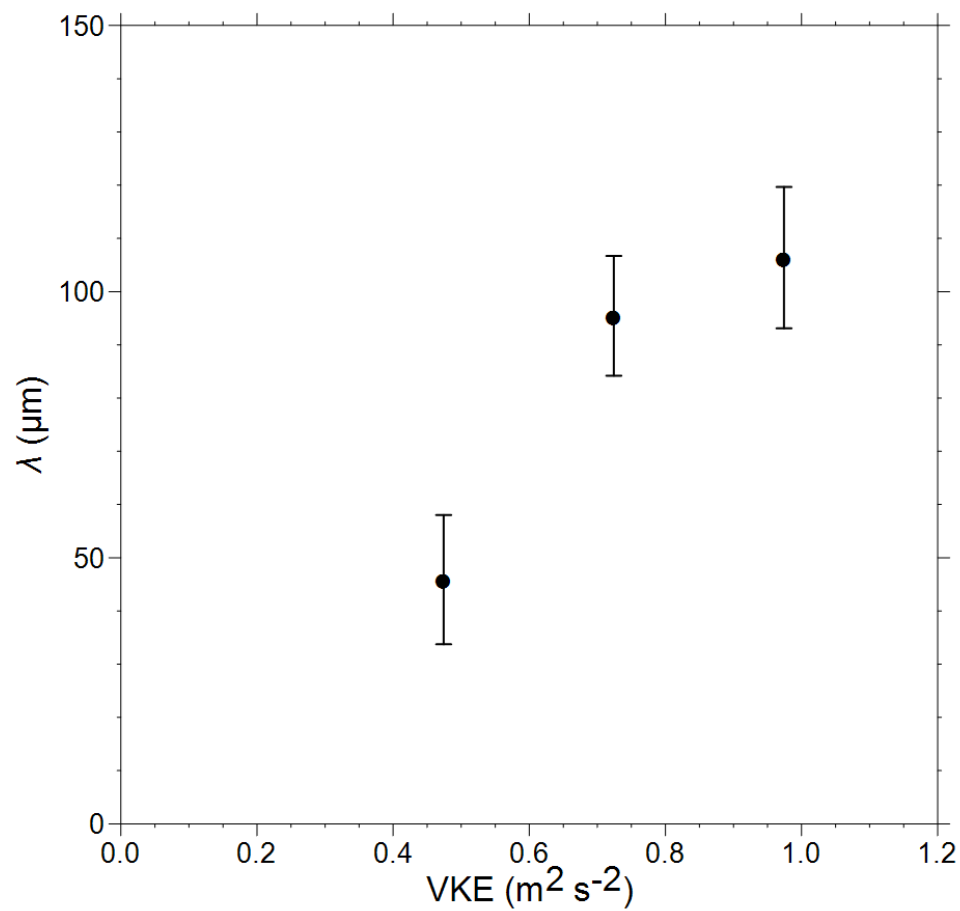
902



903

904 Figure 5. Size resolved number and mass fluxes from flights B600, B601, B602 and B610.  
 905 All plots show the gray dashed line, which indicates the range of all positive dust fluxes  
 906 measured during the flights, and the black dashed curve which is the unaltered *Kok* [2011a]  
 907 parameterization. Open circles are the measurements by [*Sow et al.*, 2009]. Colored curves  
 908 represent the same parameterization but fitted to the measurements, shown in the same  
 909 colors. For (a) and (c) each colored curve represents the average flux distribution for different  
 910 ranges vertical turbulent kinetic energy (VKE). Units of VKE in the legend are  $\text{m}^2 \text{s}^{-2}$ . For (b)

911 and (d) each curve represents the average flux distribution measured over a different  
912 geographical region. Measurements with uncertainty larger than 100 % have been omitted  
913 from the plots for clarity.



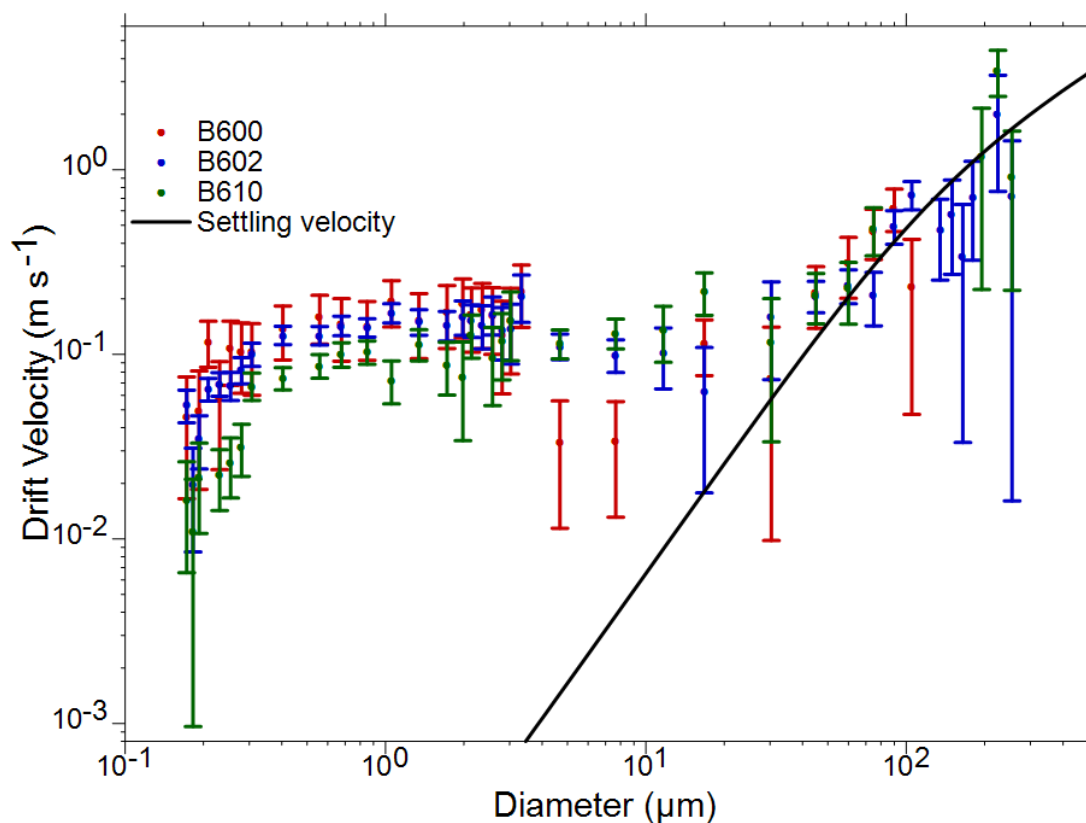
914

915 Figure 6. Variation in the parameter  $\lambda$  for the fits in Figure 5a and 5c as a function of VKE.

916

917

918

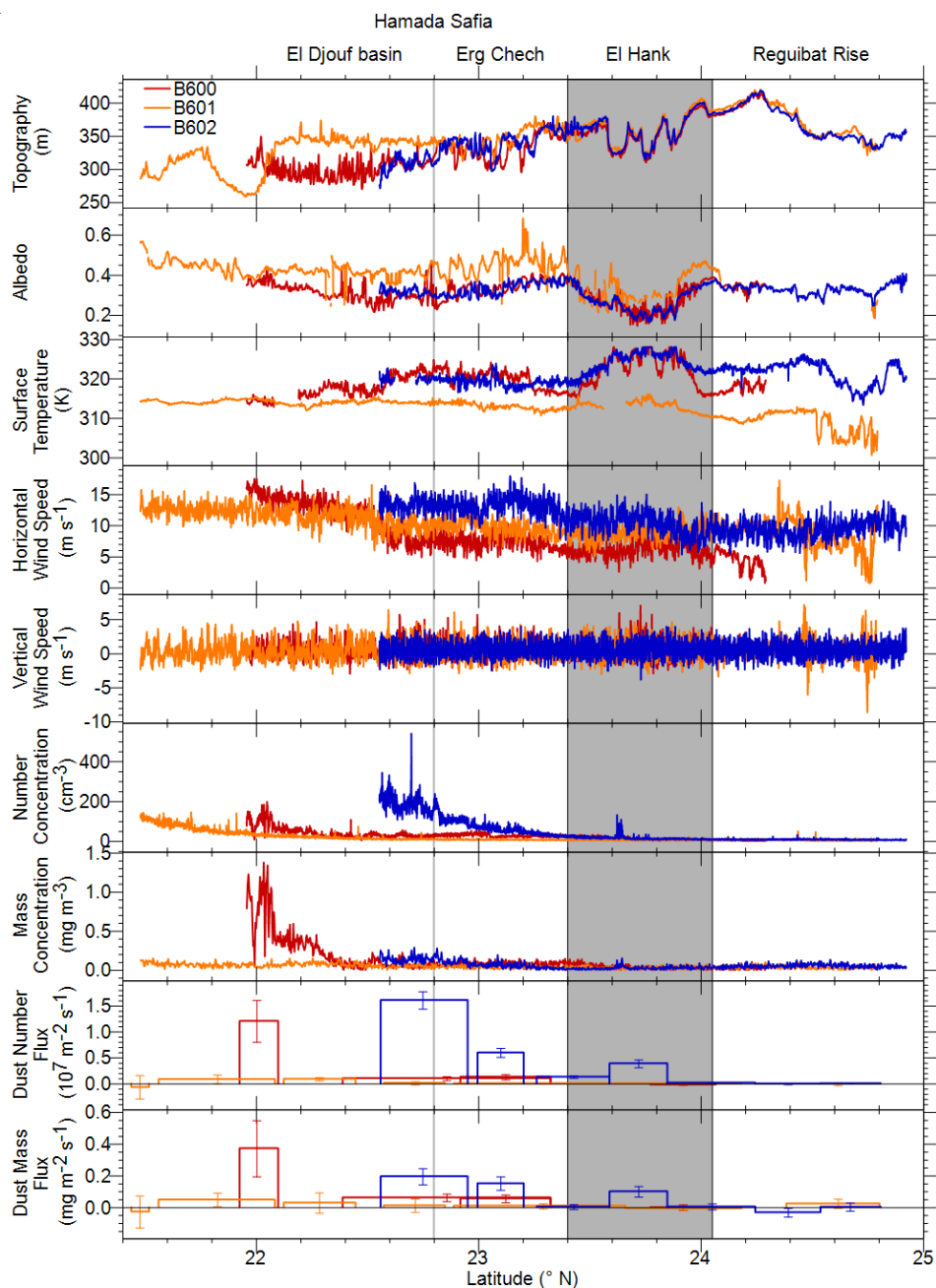


919

920 Figure 7. Drift velocity as a function of particle diameter for the peak flux measurements of  
921 flights B600, B602 and B610. Points with uncertainties greater than 100 % have been  
922 omitted. Data from Flights B601 and B613 are not shown due to their low fluxes. The line  
923 shows an estimate of the particle settling velocity. Drift velocities and settling velocities are  
924 both given positive signs for comparison despite their opposite directions.

925

926

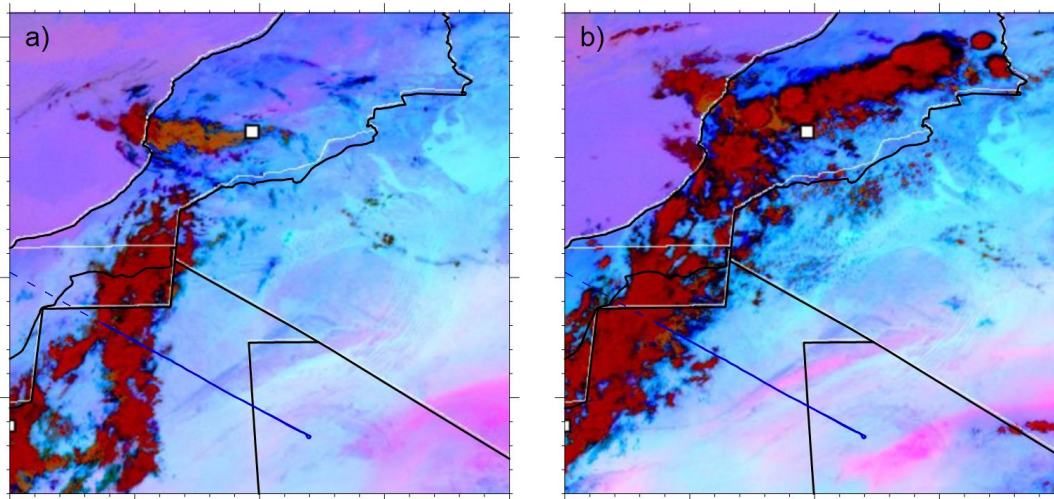


927

928 Figure 8. Data collected during long low level legs of flights B600 and B601 on 17<sup>th</sup> June  
 929 2011 and B602 on the 18<sup>th</sup> June 2011. The minimum altitude was mostly limited to 800 - 900  
 930 m due to low visibility on the 17<sup>th</sup>, however between 22.2 and 22.4° during flight B601 the  
 931 aircraft was able to briefly descend to 500 m altitude. Flight B602 was performed at  
 932 approximately 100 m altitude. All line charts are 1 s averages, except mass concentration  
 933 which is a 4 s average to reduce noise. Approximate locations of surface features are labeled  
 934 above the panels with Hamada Safia and El Hank represented by a grey line and bar  
 935 respectively.

936

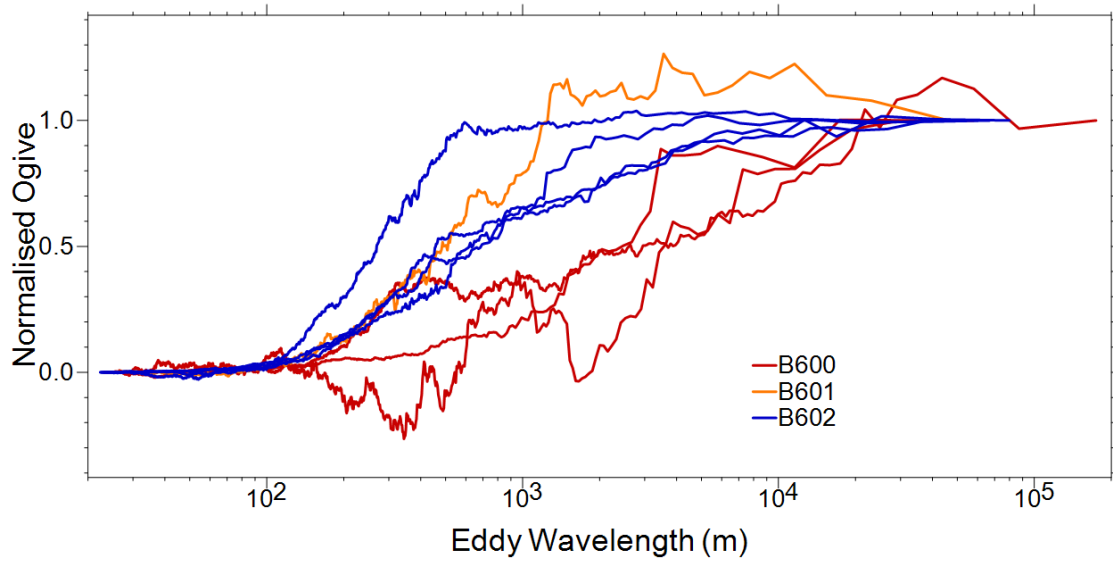




937

938 Figure 9. SEVIRI false color image for 0900 UTC (a) and 1400 UTC (b) on the day of flight  
939 B602. An increase in pinkness representing local dust uplift or upward vertical mixing of dust  
940 can be seen over El Hank and over Erg Chech at the northern edge of the El Djouf basin. The  
941 flight track for Flight B602 is overlain as per Figure 1. An animation showing the change is  
942 included as supplementary material.

943

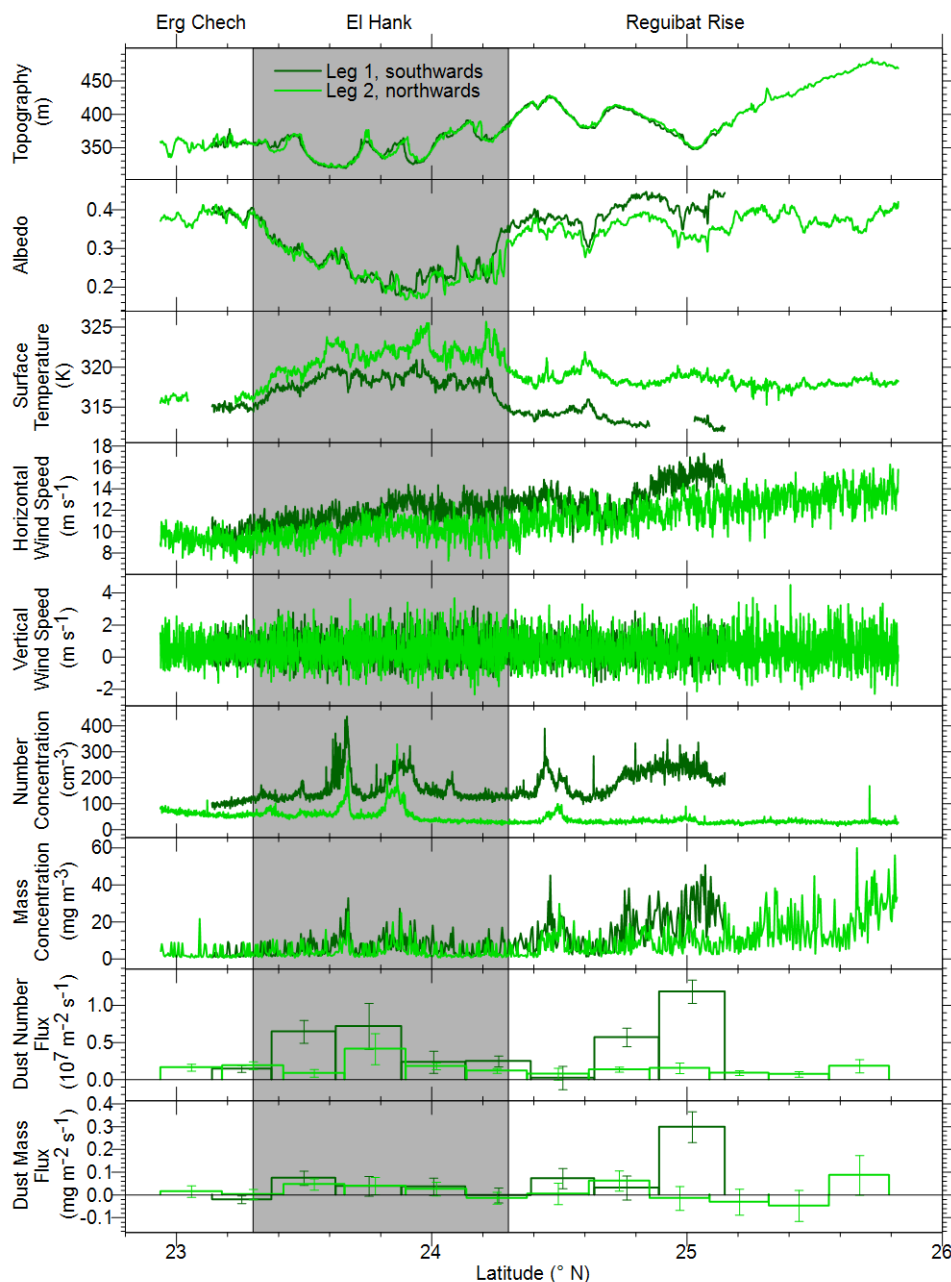


944

945 Figure 10. Ogives from flux measurements of the B600, B601 and B602 Harmattan wind  
946 cases. Each ogive represents one flux measurement and the steeper regions of the curves  
947 indicate the scales which contribute to the flux. The ogives have been normalized to unity at  
948 the largest wavelength. Ogives are only plotted for flux measurements where the uncertainty  
949 is less than 100 %, i.e. where there is a statistically significant flux.

950

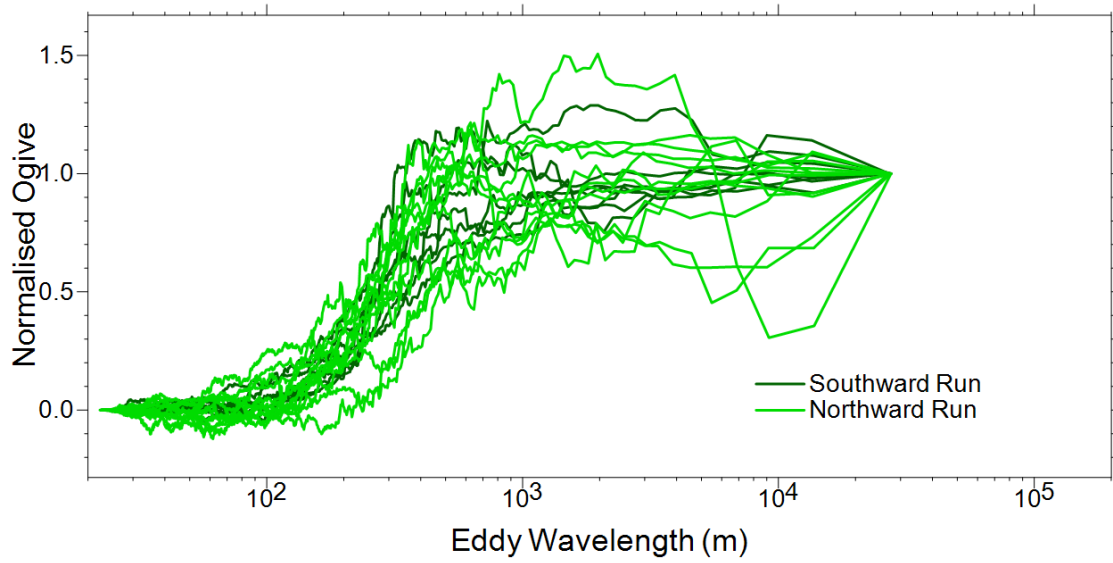
951



952

953 Figure 11 Aircraft measured parameters during the two low level legs of flight B610  
954 investigating mixing of momentum from a nocturnal low level jet. All line charts are 1 s  
955 averages, except mass concentration which is a 4 s average to reduce noise. Approximate  
956 locations of surface features are labeled above the panels with El Hank represented by a grey  
957 bar.

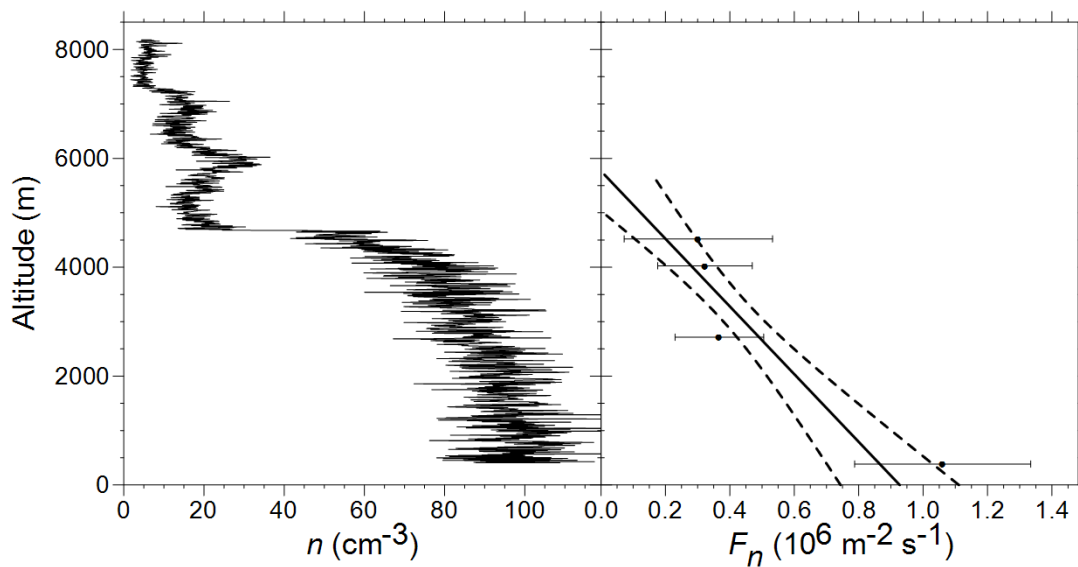
958



959

960 Figure 12. Ogives for each flux measurement of the LLJ flight B610. One ogive has been  
961 omitted because the equivalent flux measurement had a very high relative uncertainty. All  
962 curves have been normalized to unity at the largest wavelength. The steepest regions indicate  
963 the scales which contribute most to the flux.

964



965

966 Figure 13. Profile of aerosol number concentration measured during the descent made at the  
967 beginning of flight B613 and dust fluxes measured during 4 legs at different altitudes during  
968 the same flight. The solid line is a weighted linear fit and the dashed lines show the fit  
969 uncertainties.

970

971

972 **References**

- 973 Alfaro, S., A. Gaudichet, L. Gomes, and M. Maillé (1997), Modeling the size distribution of a  
974 soil aerosol produced by sandblasting, , *102(D10)*, 11239–11249.
- 975 Arnalds, O., F. O. Gísladóttir, and H. Sigurjónsson (2001), Sandy deserts of Iceland: an  
976 overview, *J. Arid Environ.*, *47(3)*, 359–371, doi:10.1006/jare.2000.0680.
- 977 Åström, J. a. (2006), Statistical models of brittle fragmentation, *Adv. Phys.*, *55(3-4)*, 247–  
978 278, doi:10.1080/00018730600731907.
- 979 Billesbach, D. P. (2011), Estimating uncertainties in individual eddy covariance flux  
980 measurements: A comparison of methods and a proposed new method, *Agric. For.*  
981 *Meteorol.*, *151(3)*, 394–405, doi:10.1016/j.agrformet.2010.12.001.
- 982 Blackadar, A. (1957), Boundary layer wind maxima and their significance for the growth of  
983 nocturnal inversions, *Bull. Am. Meteorol. Soc.*, *38(5)*, 283–290.
- 984 Blechschmidt, A.-M., J. E. Kristjánsson, H. Ólafsson, J. F. Burkhart, Ø. Hodnebrog, and P.  
985 D. Rosenberg (2012), Aircraft-based observations and high-resolution simulations of an  
986 Icelandic dust storm, *Atmos. Chem. Phys.*, *12(22)*, 10649–10666, doi:10.5194/acp-12-  
987 10649-2012.
- 988 Brindley, H., P. Knippertz, C. Ryder, and I. Ashpole (2012), A critical evaluation of the  
989 ability of the Spinning Enhanced Visible and Infrared Imager (SEVIRI) thermal infrared  
990 red-green-blue rendering to identify dust events: Theoretical analysis, *J. Geophys. Res.*,  
991 *117*, D07201, doi:10.1029/2011JD017326.
- 992 Brooks, I., and D. Rogers (2000), Aircraft observations of the mean and turbulent structure of  
993 a shallow boundary layer over the Persian Gulf, *Boundary-layer Meteorol.*, *95(2)*, 189–  
994 210.
- 995 Cuesta, J., J. H. Marsham, D. J. Parker, and C. Flamant (2009), Dynamical mechanisms  
996 controlling the vertical redistribution of dust and the thermodynamic structure of the  
997 West Saharan atmospheric boundary layer during summer, *Atmos. Sci. Lett.*, *10(1)*, 34–  
998 42, doi:10.1002/asl.207.
- 999 Davies, T., M. J. P. Cullen, a. J. Malcolm, M. H. Mawson, a. Staniforth, a. a. White, and N.  
1000 Wood (2005), A new dynamical core for the Met Office’s global and regional modelling  
1001 of the atmosphere, *Q. J. R. Meteorol. Soc.*, *131(608)*, 1759–1782, doi:10.1256/qj.04.101.
- 1002 Dorsey, J. R., E. Nemitz, M. W. Gallagher, D. Fowler, P. I. Williams, K. N. Bower, and K.  
1003 M. Beswick (2002), Direct measurements and parameterisation of aerosol flux,  
1004 concentration and emission velocity above a city, *Atmos. Environ.*, *36(5)*, 791–800,  
1005 doi:10.1016/S1352-2310(01)00526-X.
- 1006 Drexler, J. M., A. D. Gledhill, K. Shinoda, A. L. Vasiliev, K. M. Reddy, S. Sampath, and N.  
1007 P. Padture (2011), Jet engine coatings for resisting volcanic ash damage., *Adv. Mater.*,  
1008 *23(21)*, 2419–24, doi:10.1002/adma.201004783.

- 1009 Egan, B. A. (1984), Transport and diffusion in complex terrain, *Boundary-Layer Meteorol.*,  
1010 30, 3–28.
- 1011 Fiedler, S., K. Schepanski, B. Heinold, P. Knippertz, and I. Tegen (2013), Climatology of  
1012 nocturnal low-level jets over North Africa and implications for modeling mineral dust  
1013 emission, *J. Geophys. Res. Atmos.*, 118(12), 6100–6121, doi:10.1002/jgrd.50394.
- 1014 Gillette, D. A. (1974), On the production of soil wind erosion having the potential for long  
1015 range transport, *J. Rech. Atmos.*, 8, 734–744.
- 1016 Gillette, D. A., I. H. Blifford Jr., and C. R. Fenster (1972), Measurements of Aerosol Size  
1017 Distributions and Vertical Fluxes of Aerosols on Land Subject to Wind Erosion.pdf, *J.*  
1018 *Appl. Meteorol.*, 11, 977–987.
- 1019 Gillette, D. A., I. H. Blifford, and D. W. Fryrear (1974), The influence of wind velocity on  
1020 the size distributions of aerosols generated by the wind erosion of soils, *J. Geophys.*  
1021 *Res.*, 79(27), 4068–4075.
- 1022 Heinold, B., P. Knippertz, J. H. Marsham, S. Fiedler, N. S. Dixon, K. Schepanski, B. Laurent,  
1023 and I. Tegen (2013), The role of deep convection and nocturnal low-level jets for dust  
1024 emission in summertime West Africa: Estimates from convection-permitting  
1025 simulations, *J. Geophys. Res. Atmos.*, 118(10), 4385–4400, doi:10.1002/jgrd.50402.
- 1026 Hobby, M., M. Gascoyne, J. H. Marsham, M. Bart, C. Allen, S. Engelstaedter, D. M. Fadel,  
1027 A. Gandega, R. Lane, J. B. McQuaid, B. Ouchene, A. Ouladichir, D. J. Parker, P.  
1028 Rosenberg, M. S. Ferroudj, A. Saci, F. Seddik, M. Todd, D. Walker, and R. Washington  
1029 (2013), The Fennec Automatic Weather Station (AWS) Network: Monitoring the  
1030 Saharan Climate System, *J. Atmos. Ocean. Technol.*, 30(4), 709–724,  
1031 doi:10.1175/JTECH-D-12-00037.1.
- 1032 Huang, Q., J. H. Marsham, D. J. Parker, W. Tian, and C. M. Grams (2010), Simulations of  
1033 the effects of surface heat flux anomalies on stratification, convective growth, and  
1034 vertical transport within the Saharan boundary layer, *J. Geophys. Res.*, 115, D05201,  
1035 doi:10.1029/2009JD012689.
- 1036 Huneus, N., M. Schulz, Y. Balkanski, J. Griesfeller, J. Prospero, S. Kinne, S. Bauer, O.  
1037 Boucher, M. Chin, F. Dentener, T. Diehl, R. Easter, D. Fillmore, S. Ghan, P. Ginoux, a.  
1038 Grini, L. Horowitz, D. Koch, M. C. Krol, W. Landing, X. Liu, N. Mahowald, R. Miller,  
1039 J.-J. Morcrette, G. Myhre, J. Penner, J. Perlwitz, P. Stier, T. Takemura, and C. S. Zender  
1040 (2011), Global dust model intercomparison in AeroCom phase I, *Atmos. Chem. Phys.*,  
1041 11(15), 7781–7816, doi:10.5194/acp-11-7781-2011.
- 1042 Kaufman, Y. J., I. Koren, L. A. Remer, D. Tanré, P. Ginoux, and S. Fan (2005), Dust  
1043 transport and deposition observed from the Terra-Moderate Resolution Imaging  
1044 Spectroradiometer (MODIS) spacecraft over the Atlantic Ocean, *J. Geophys. Res.*,  
1045 110(D10), D10S12, doi:10.1029/2003JD004436.
- 1046 Knippertz, P. (2008), Dust emissions in the West African heat trough - the role of the diurnal  
1047 cycle and of extratropical disturbances, *Meteorol. ZEITSCHRIFT*, 17(5), 553–563,  
1048 doi:10.1127/0941-2948/2008/0315.

- 1049 Kocha, C., P. Tulet, J.-P. Lafore, and C. Flamant (2013), The importance of the diurnal cycle  
1050 of Aerosol Optical Depth in West Africa, *Geophys. Res. Lett.*, *40*(4), 785–790,  
1051 doi:10.1002/grl.50143.
- 1052 Koehler, K. a., S. M. Kreidenweis, P. J. DeMott, M. D. Petters, a. J. Prenni, and C. M.  
1053 Carrico (2009), Hygroscopicity and cloud droplet activation of mineral dust aerosol,  
1054 *Geophys. Res. Lett.*, *36*, L08805, doi:10.1029/2009GL037348.
- 1055 Kok, J. F. (2011a), A scaling theory for the size distribution of emitted dust aerosols suggests  
1056 climate models underestimate the size of the global dust cycle., *Proc. Natl. Acad. Sci. U.*  
1057 *S. A.*, *108*(3), 1016–1021, doi:10.1073/pnas.1014798108.
- 1058 Kok, J. F. (2011b), Does the size distribution of mineral dust aerosols depend on the wind  
1059 speed at emission?, *Atmos. Chem. Phys.*, *11*(19), 10149–10156, doi:10.5194/acp-11-  
1060 10149-2011.
- 1061 Kok, J. F., E. J. R. Parteli, T. I. Michaels, and D. B. Karam (2012), The physics of wind-  
1062 blown sand and dust, *Reports Prog. Phys.*, *75*(10), 106901, doi:10.1088/0034-  
1063 4885/75/10/106901.
- 1064 Lock, A. . P., A. R. Brown, M. R. Bush, G. M. Martin, and R. N. B. Smith (2000), A new  
1065 boundary layer mixing scheme. Part I: Scheme description and single-column model  
1066 tests., *Mon. Weather Rev.*, (1998), 3187–3199.
- 1067 Marsham, J., P. Knippertz, N. Dixon, D. J. Parker, and G. M. S. Lister (2011), The  
1068 importance of the representation of deep convection for modeled dust-generating winds  
1069 over West Africa during summer, *Geophys. Res. Lett.*, *38*, L16803,  
1070 doi:10.1029/2011GL048368.
- 1071 Marsham, J. H., D. J. Parker, C. M. Grams, B. T. Johnson, W. M. F. Grey, and a. N. Ross  
1072 (2008), Observations of mesoscale and boundary-layer scale circulations affecting dust  
1073 transport and uplift over the Sahara, *Atmos. Chem. Phys.*, *8*(23), 6979–6993.
- 1074 Marsham, J. H., M. Hobby, C. J. T. Allen, J. R. Banks, M. Bart, B. J. Brooks, C. Cavazos-  
1075 Guerra, S. Engelstaedter, M. Gascoyne, a. R. Lima, J. V. Martins, J. B. McQuaid, A.  
1076 O’Leary, B. Ouchene, A. Ouladichir, D. J. Parker, A. Saci, M. Salah-Ferroudj, M. C.  
1077 Todd, and R. Washington (2013), Meteorology and dust in the central Sahara:  
1078 Observations from Fennec supersite-1 during the June 2011 Intensive Observation  
1079 Period, *J. Geophys. Res.*, *118*, doi:10.1002/jgrd.50211.
- 1080 May, P. T. (1995), The Australian nocturnal jet and diurnal variations of boundary-layer  
1081 winds over Mt. Isa in north-eastern Australia, *Q. J. R. Meteorol. Soc.*, *121*(525), 987–  
1082 1003, doi:10.1002/qj.49712152503.
- 1083 McConnell, C. L., E. J. Highwood, H. Coe, P. Formenti, B. Anderson, S. Osborne, S. Nava,  
1084 K. Desboeufs, G. Chen, and M. a. J. Harrison (2008), Seasonal variations of the physical  
1085 and optical characteristics of Saharan dust: Results from the Dust Outflow and  
1086 Deposition to the Ocean (DODO) experiment, *J. Geophys. Res.*, *113*, D14S05,  
1087 doi:10.1029/2007JD009606.



- 1088 Netoff, D. I., and M. A. Chan (2009), Aeolian activity at a giant sandstone weathering pit in  
1089 arid south-central Utah, *Earth Surf. Process. Landforms*, *34*, 99–108, doi:10.1002/esp.
- 1090 Oerlemans, J., R. H. Giesen, and M. R. Van Den Broeke (2009), Retreating alpine glaciers:  
1091 increased melt rates due to accumulation of dust (Vadret da Morteratsch, Switzerland),  
1092 *J. Glaciol.*, *55*(192), 729–736, doi:10.3189/002214309789470969.
- 1093 Painter, T. H., A. P. Barrett, C. C. Landry, J. C. Neff, M. P. Cassidy, C. R. Lawrence, K. E.  
1094 McBride, and G. L. Farmer (2007), Impact of disturbed desert soils on duration of  
1095 mountain snow cover, *Geophys. Res. Lett.*, *34*(12), L12502,  
1096 doi:10.1029/2007GL030284.
- 1097 Park, S.-U., and E.-H. Lee (2004), Parameterization of Asian dust (Hwangsa) particle-size  
1098 distributions for use in dust emission models, *Atmos. Environ.*, *38*(14), 2155–2162,  
1099 doi:10.1016/j.atmosenv.2004.01.024.
- 1100 Petersen, G. N., and I. A. Renfrew (2009), Aircraft-based observations of air – sea fluxes  
1101 over Denmark Strait and the Irminger Sea during high wind speed conditions, *Q. J. R.*  
1102 *Meteorol. Soc.*, *135*(645), 2030–2045, doi:10.1002/qj.
- 1103 Prata, A. J., and A. Tupper (2009), Aviation hazards from volcanoes: the state of the science,  
1104 *Nat. Hazards*, *51*(2), 239–244, doi:10.1007/s11069-009-9415-y.
- 1105 Prospero, J. M., J. E. Bullard, and R. Hodgkins (2012), High-latitude dust over the North  
1106 Atlantic: inputs from Icelandic proglacial dust storms., *Science (80-. )*, *335*(6072),  
1107 1078–1082, doi:10.1126/science.1217447.
- 1108 Reto, S., E. Vermote, N. Saleous, R. Simmon, and D. Herring (2005), *The Blue Marble Next*  
1109 *Generation - A true color earth dataset including seasonal dynamics from MODIS*,  
1110 NASA Earth Observatory.
- 1111 Rosenberg, P. D., A. R. Dean, P. I. Williams, J. R. Dorsey, A. Minikin, M. A. Pickering, and  
1112 A. Petzold (2012), Particle sizing calibration with refractive index correction for light  
1113 scattering optical particle counters and impacts upon PCASP and CDP data collected  
1114 during the Fennec campaign, *Atmos. Meas. Tech.*, *5*(5), 1147–1163, doi:10.5194/amt-5-  
1115 1147-2012.
- 1116 Ryder, C. L., E. J. Highwood, T. M. Lai, H. Sodemann, and J. H. Marsham (2013a), Impact  
1117 of atmospheric transport on the evolution of microphysical and optical properties of  
1118 Saharan dust, *Geophys. Res. Lett.*, *40*(10), 2433–2438, doi:10.1002/grl.50482.
- 1119 Ryder, C. L., E. J. Highwood, P. D. Rosenberg, J. Trembath, J. K. Brooke, M. Bart, A. Dean,  
1120 J. Crosier, J. Dorsey, H. Brindley, J. Banks, J. H. Marsham, J. B. McQuaid, H.  
1121 Sodemann, and R. Washington (2013b), Optical properties of Saharan dust aerosol and  
1122 contribution from the coarse mode as measured during the Fennec 2011 aircraft  
1123 campaign, *Atmos. Chem. Phys.*, *13*(1), 303–325, doi:10.5194/acp-13-303-2013.
- 1124 Schatz, V., and H. J. Herrmann (2006), Flow separation in the lee side of transverse dunes: A  
1125 numerical investigation, *Geomorphology*, *81*(1-2), 207–216,  
1126 doi:10.1016/j.geomorph.2006.04.009.

- 1127 Schepanski, K., I. Tegen, M. C. Todd, B. Heinold, G. Bönisch, B. Laurent, and a. Macke  
1128 (2009), Meteorological processes forcing Saharan dust emission inferred from MSG-  
1129 SEVIRI observations of subdaily dust source activation and numerical models, *J.*  
1130 *Geophys. Res.*, *114*(D10), D10201, doi:10.1029/2008JD010325.
- 1131 Schepanski, K., C. Flamant, J.-P. Chaboureaud, C. Kocha, J. R. Banks, H. E. Brindley, C.  
1132 Lavaysse, F. Marnas, J. Pelon, and P. Tulet (2013), Characterization of dust emission  
1133 from alluvial sources using aircraft observations and high-resolution modeling, *J.*  
1134 *Geophys. Res. Atmos.*, *118*(13), 7237–7259, doi:10.1002/jgrd.50538.
- 1135 Shao, Y. (2001), A model for mineral dust emission, *J. Geophys. Res.*, *106*(D17), 20239–  
1136 20254, doi:10.1029/2001JD900171.
- 1137 Shao, Y. (2008), *Physics and Modelling of Wind Erosion*, 2nd ed., Springer.
- 1138 Shin, H. H., and S.-Y. Hong (2013), Analysis of Resolved and Parameterized Vertical  
1139 Transports in Convective Boundary Layers at Gray-Zone Resolutions, *J. Atmos. Sci.*,  
1140 *70*(10), 3248–3261, doi:10.1175/JAS-D-12-0290.1.
- 1141 Shpund, J., M. Pinsky, and a. Khain (2011), Microphysical Structure of the Marine Boundary  
1142 Layer under Strong Wind and Spray Formation as Seen from Simulations Using a 2D  
1143 Explicit Microphysical Model. Part I: The Impact of Large Eddies, *J. Atmos. Sci.*,  
1144 *68*(10), 2366–2384, doi:10.1175/2011JAS3652.1.
- 1145 Sodemann, H., A. S. Palmer, C. Schwierz, M. Schwikowski, and H. Wernli (2006), The  
1146 transport history of two Saharan dust events archived in an Alpine ice core, *Atmos.*  
1147 *Chem. Phys.*, *6*(3), 667–688.
- 1148 Solomos, S., G. Kallos, E. Mavromatidis, and J. Kushta (2012), Density currents as a desert  
1149 dust mobilization mechanism, *Atmos. Chem. Phys.*, *12*(22), 11199–11211,  
1150 doi:10.5194/acp-12-11199-2012.
- 1151 Sow, M., S. Alfaro, J. Rojot, and B. Marticorena (2009), Size resolved dust emission fluxes  
1152 measured in Niger during 3 dust storms of the AMMA experiment, *Atmos. Chem. Phys.*,  
1153 *9*(12), 3881–3891.
- 1154 Stuart, A. (1927), On a Black Sand from South-East Iceland, *Geol. Mag.*, *64*(12), 540–545,  
1155 doi:10.1017/S0016756800103899.
- 1156 Stull, R. B. (1988), *An Introduction to Boundary Layer Meteorology*, Kluwer Academic  
1157 Publishers, Dordrecht / Boston / London.
- 1158 Sun, D., K. M. Lau, and M. Kafatos (2008), Contrasting the 2007 and 2005 hurricane  
1159 seasons: Evidence of possible impacts of Saharan dry air and dust on tropical cyclone  
1160 activity in the Atlantic basin, *Geophys. Res. Lett.*, *35*(15), L15405,  
1161 doi:10.1029/2008GL034529.
- 1162 Tegen, I., and I. Fung (1994), Modeling of mineral dust in the atmosphere: Sources,  
1163 transport, and optical thickness, *J. Geophys. Res.*, *99*(D11), 22897–22914.

- 1164 Todd, M. C., C. J. T. Allen, M. Bart, M. Bechir, J. Bentefouet, B. J. Brooks, C. Cavazos-  
1165 Guerra, T. Clovis, S. Deyane, M. Dieh, S. Engelstaedter, C. Flamant, L. Garcia-  
1166 Carreras, a. Gandega, M. Gascoyne, M. Hobby, C. Kocha, C. Lavaysse, J. H. Marsham,  
1167 J. V. Martins, J. B. McQuaid, J. B. Ngamini, D. J. Parker, T. Podvin, a. Rocha-Lima, S.  
1168 Traore, Y. Wang, and R. Washington (2013), Meteorological and dust aerosol  
1169 conditions over the western Saharan region observed at Fennec Supersite-2 during the  
1170 intensive observation period in June 2011, *J. Geophys. Res. Atmos.*, 118(15), 8426–  
1171 8447, doi:10.1002/jgrd.50470.
- 1172 Washington, R., M. C. Todd, G. Lizcano, I. Tegen, C. Flamant, I. Koren, P. Ginoux, S.  
1173 Engelstaedter, C. S. Bristow, C. S. Zender, a. S. Goudie, A. Warren, and J. M. Prospero  
1174 (2006), Links between topography, wind, deflation, lakes and dust: The case of the  
1175 Bodélé Depression, Chad, *Geophys. Res. Lett.*, 33, L09401,  
1176 doi:10.1029/2006GL025827.
- 1177 Van de Wiel, B. J. H., A. F. Moene, G. J. Steeneveld, P. Baas, F. C. Bosveld, and A. A. M.  
1178 Holtslag (2010), A Conceptual View on Inertial Oscillations and Nocturnal Low-Level  
1179 Jets, *J. Atmos. Sci.*, 67(8), 2679–2689, doi:10.1175/2010JAS3289.1.
- 1180 Wyngaard, J. C. (2004), Toward Numerical Modeling in the ““Terra Incognita,”” *J. Atmos.*  
1181 *Sci.*, 61(14), 1816–1826.
- 1182 Zhao, C., X. Liu, and L. R. Leung (2012), Impact of the Desert dust on the summer monsoon  
1183 system over Southwestern North America, *Atmos. Chem. Phys.*, 12(8), 3717–3731,  
1184 doi:10.5194/acp-12-3717-2012.
- 1185